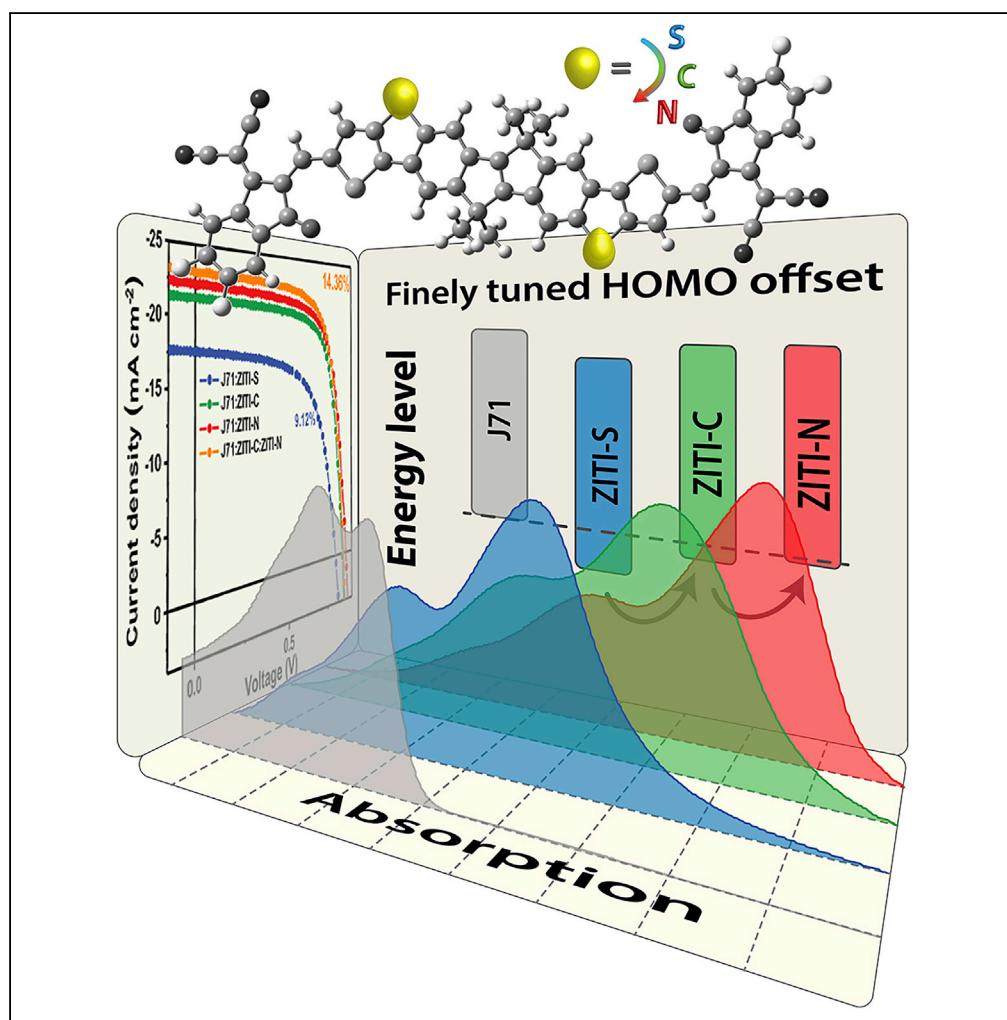## Article

Revealing the Critical Role of the HOMO Alignment on Maximizing Current Extraction and Suppressing Energy Loss in Organic Solar Cells

Jianyun Zhang, Wenrui Liu, Ming Zhang, ..., Haiming Zhu, Feng Liu, Xiaozhang Zhu

xushengjie@iccas.ac.cn (S.X.)
fengliu82@sjtu.edu.cn (F.L.)
xzzhu@iccas.ac.cn (X.Z.)

HIGHLIGHTS

NIR acceptors with high structural similarity and variable HOMO levels were designed

We achieved the highest PCE of 14.36% by combining J71, ZITI-C, and ZITI-N acceptors

We revealed the importance of the optimized driving force on the device performance

Article

Revealing the Critical Role of the HOMO Alignment on Maximizing Current Extraction and Suppressing Energy Loss in Organic Solar Cells

Jianyun Zhang,[1,2,6] Wenrui Liu,[1,2,6] Ming Zhang,[4,6] Yanfeng Liu,[3] Guanqing Zhou,[4] Shengjie Xu,[1,*] Fengling Zhang,[3] Haiming Zhu,[5] Feng Liu,[4,*] and Xiaozhang Zhu[1,2,7,*]

SUMMARY

For state-of-the-art organic solar cells (OSCs) consisting of a large-bandgap polymer donor and a near-infrared (NIR) molecular acceptor, the control of the HOMO offset is the key to simultaneously achieve small energy loss (E_{loss}) and high photocurrent. However, the relationship between HOMO offsets and the efficiency for hole separation is quite elusive so far, which requires a comprehensive understanding on how small the driving force can effectively perform the charge separation while obtaining a high photovoltage to ensure high OSC performance. By designing a new family of ZITI-X NIR acceptors (X = S, C, N) with a high structural similarity and matching them with polymer donor J71 forming reduced HOMO offsets, we systematically investigated and established the relationship among the photovoltaic performance, energy loss, and hole-transfer kinetics. We achieved the highest PCE$_{avg}$s of 14.05 $\pm$ 0.21% in a ternary system (J71:ZITI-C:ZITI-N) that best optimize the balance between driving force and energy loss.

INTRODUCTION

Organic solar cells (OSCs) with a bulk heterojunction (BHJ) structure that respond to a wide solar spectrum and collect carriers with low energy loss have attracted significant attention owing to the quick improvement in device efficiency (Yu et al., 1995; Lu et al., 2015; Kang et al., 2016). The core issue is how to simultaneously achieve small energy loss (Vandewal et al., 2009; Yao et al., 2015) [$E_{loss} = E_{gap}-qV_{oc}$, where E_{gap} is the optical bandgap, V_{oc} is the open-circuit voltage and q is elementary charge.] and keep a high photocurrent. Recent progress shows success of using non-fullerene acceptors to extend thin-film absorption, while keeping a low energy loss, achieving a balanced trade-off between V_{oc} and J_{sc} (short-circuit current) to enhance power conversion efficiency (Qian et al., 2018; Menke et al., 2018; Sun et al., 2018; Zhang et al., 2018a, 2018b; 2018c; Xie et al., 2018; Nian et al., 2018; Fei et al., 2018; Yuan et al., 2019; Yu et al., 2019; Liu et al., 2019; Cui et al., 2019). D-A-type non-fullerene acceptors (NFAs) have shown distinct advantages of highly tunable absorption and molecular energy level (Zhang et al., 2018a, 2018b; 2018c; Yan et al., 2018; Wadsworth et al., 2019; Cheng et al., 2018), which also exhibit efficient charge separation at a low driving force (Liu et al., 2016), a unique opportunity to minimize the V_{oc}-J_{sc} trade-off. Within such scenario, maximum power conversion efficiency (PCE) for NFA-based single-junction OSCs is predicted to be 19% with an absorption onset at ∼860 nm and a low non-radiative recombination loss of ∼0.21 V (Hou et al., 2018).

State-of-the-art NFA-based OSCs contain wide/medium-bandgap donors and near-infrared (NIR) NFAs forming a complementary absorption. NIR NFAs are normally designed by introducing strong electron-accepting terminals or electron-donating bulky core to enhance intramolecular charge transfer property (Li et al., 2018a, 2018b; Kan et al., 2017, 2018; Liu et al., 2017). A successful example can be seen from IT-4F (Zhao et al., 2017), which shows downshifted lowest unoccupied molecular orbital (LUMO) energy level and redshifted absorption compared with ITIC (Lin et al., 2015) owing to the addition of INCN-2F onto IDTT core. By matching with polymer donor PBDB-TF, IT-4F-based devices (Li et al., 2018b) show a higher average power conversion efficiency (PCE$_{avg}$) of 13.30 $\pm$ 0.20%, however, with an undesirably higher E_{loss}, 0.66 eV, compared with ITIC-based devices (Yu et al., 2018) with a PCE$_{avg}$ of 10.0 $\pm$ 0.1% and an E_{loss} of 0.58 eV. Such dilemma is common in NIR NFA materials design. The bandgap that is associated with J_{sc} is on the contrary to energy loss reduction. The calculation of energy loss is based on NFA components featuring narrower optical bandgaps, and the E_{loss} can be reduced via the proper highest occupied

molecular orbital (HOMO) regulation (Yao et al., 2016) at the stake of reducing the driving force for hole transfer defined by the energy difference between the optical bandgap of NIR NFAs and the energy of the charge transfer (CT) state in the blends (E_{gap}^{NFA}-E_{CT}). A good demonstration can be seen from the comparison between BT-IC and BDT-IC (Kan et al., 2017; Li et al., 2017a, 2017b). BT-IC shows a higher HOMO energy level than BDT-IC, −5.32 eV versus −5.51 eV. By matching a wide-bandgap polymer J71, BT-IC-based OSCs delivered a much lower E_{loss} of 0.53 eV than BDT-IC (E_{loss}: 0.61 eV). Currently, Yan et al. reported very low energy offsets between PffBT2T-TT donor and O-IDTBR acceptor delivering a maximum PCE of 10.4% (Chen et al., 2018) but only with a moderate maximum external quantum efficiency (EQE$_{max}$) of 67%. Thus, sufficient driving force should be guaranteed to ensure efficient charge separation to achieve the best OSC performance. However, as indicated in Figure S10 and Table S8 that summarized the EQE$_{max}$s in NIR region against HOMO offsets for the reported OSCs with efficiencies over 12%, the relationship between HOMO offsets and the efficiency for hole separation is quite elusive so far, which can be attributed to the difficulty in decoupling the impacts originating from the blend morphology. To achieve the most optimized materials combination and the best device performance, we need a comprehensive understanding on how small a driving force can effectively perform the charge separation while obtaining a high photovoltage to ensure high OSC performance (Cha et al., 2018), a picture that is of particular importance to guide materials design to ensure low E_{loss} and high EQE, which is highly challenging without an ideal research model system and is the target of this work.

When designing A-D-A-type NFAs, the bulky electron-donating core based on fused heteroarenes determines the HOMO energy level. The bridging heteroatoms are effective to modulate the electron-donating ability of fused heteroarenes in terms of their various electronegativity, aromaticity, and σ-π conjugation effect (Yamaguchi and Tamao, 2015). Such protocol enables us to fine-tune the energy level of NIR NFAs. We recently developed indenoindene-based NIR acceptors NITI (Xu et al., 2017) and ZITI (Liu et al., 2018a) that exhibit high PCEs over 13% (Zhou et al., 2018). In this work, we manipulated NIR NFAs synthesized by introducing heteroatom bridge, yielding ZITI-S, ZITI-C, and ZITI-N, with precise control over HOMO energy levels and NIR absorptions. Theoretical calculation is useful to predict the variation trend of photoelectric properties in conjugated materials. Density functional theory (DFT) calculations (Figure 1) show that the backbone introduction of heteroatoms is an effective method in modulating HOMO energy level, whereas the LUMO energy level depends more on acceptor moieties. Despite the reduced optical bandgap from ZITI-S (1.61 eV), ZITI-C (1.47 eV) to ZITI-N (1.41 eV), J71:ZITI-S-, J71:ZITI-C-, and J71:ZITI-N-based solar cells show gradually increased V_{oc}s of 0.812 ± 0.004, 0.851 ± 0.006, and 0.873 ± 0.005 V with E_{loss}s of 0.80, 0.62, and 0.53 eV. Such materials provide a good platform to investigate the detailed correlations among E_{loss}, EQE, and driving force. We show that a moderate driving force down to ∼100 meV can ensure efficient charge transfer to achieve high short-circuit current. Such value in couple with energy loss pictures the fundamental physics of charge separation and energy level alignment at donor-acceptor interfaces. Detailed manipulation of hole transfer energy levels of combining double acceptor BHJ blends yielded a high PCE of 14.05 ± 0.21%. Thus, minimizing trade-off between charge transfer driving force and short-circuit current is an effective methodology that needs to be highlighted in both materials design and device optimization to ensure low E_{loss} and high PCE.

RESULTS AND DISCUSSION

Materials Design and Photoelectric Property

Figure 1 shows the structures and DFT calculations of heteroatom bridged IIDTs. It is seen that the frontier energy levels of IIDT-X can be well controlled by selecting S, C, N bridge atoms. The HOMO of the resulting NFAs is located at IIDT-X center, and the LUMO is located at INCN-2F moieties. Thus, gradually changed HOMO energy levels and similar LUMO energy levels are expected for ZITI-X series. Detailed synthesis for ZITI-S, ZITI-C, and ZITI-N is shown in Supplemental Information. These acceptors show good thermal stability with high thermal decomposition temperatures of 318°C, 321°C, and 323°C for ZITI-S, ZITI-C, and ZITI-N, respectively (see Figure S1). The photophysical and electrochemical properties of ZITI-X acceptors are examined. The absorption spectra of J71 donor and ZITI-X acceptors in thin films are shown in Figure 2A. ZITI-S, ZITI-C, and ZITI-N exhibit maximum absorptions at 677, 717, and 747 nm with high molar extinction coefficients (ε) of 2.11 × 10^5, 2.46 × 10^5, and 2.90 × 10^5 M^{-1} cm^{-1} in solution, respectively (see Figure S2), and broad NIR absorptions between 500 and 900 nm with absorption peaks at 709, 756, and 798 nm in thin films that are redshifted by 32, 39, and 51 nm. The optical bandgaps of ZITI-S, ZITI-C, and ZITI-N are estimated to be 1.61, 1.47, and 1.41 eV based on absorption onsets. Frontier orbital energy levels of ZITI-X are determined by cyclic voltammetry (see Figure S2), and the energy diagram including J71
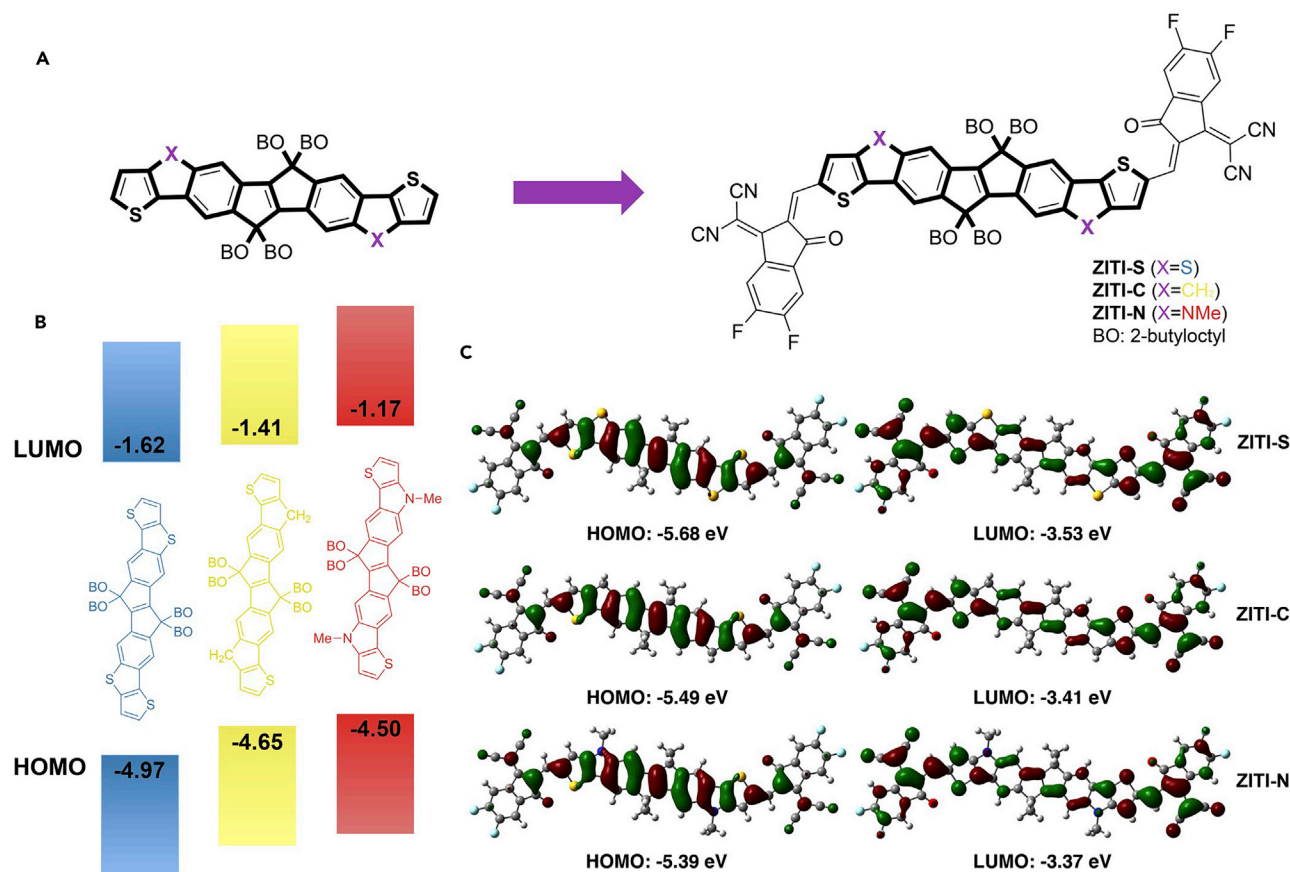
Figure 1. Chemical Structures and Energy-Level Alignment

(A) The molecular structures of IIDT-X and ZITI-X.

(B) Energy-level evolution of heteroarenes IIDT-S, IIDT-C, and IIDT-N by DFT calculations at B3LYP/6-31G** level.

(C) Optimized geometries and contour plots of frontier molecular orbitals with HOMO and LUMO energy levels of ZITI-X NFAs.

donor is presented in Figure 2B. The HOMO and LUMO energy levels are calculated from onsets of oxidation and reduction processes that are calibrated by ferrocene/ferrocenium. ZITI-S, ZITI-C, and ZITI-N show slightly different LUMOs of -3.87, -3.81, and -3.82 eV, but significantly up-shifted HOMOs of -5.80, -5.65 to -5.53 eV, respectively. Thus, the HOMO offsets between ZITI-X and J71 (HOMO: -5.48 eV) gradually decrease for S, C, N molecules, suggesting reduced hole side driving force. As shown in Figure S3, the J71:ZITI-S, J71:ZITI-C, and J71:ZITI-N blends show high photoluminescence quenching efficiency indicating efficient charge separation.

Photovoltaic Characterization of ZITI-X-Based Devices

The conventional device architecture of ITO/PEDOT:PSS/active layer/PDINO/Al is adopted to evaluate photovoltaic performance of these acceptors. We screened the donor-acceptor (D-A) weight ratio and the temperature for thermal annealing treatment. Detailed photovoltaic parameters are summarized in Tables S1–S3. We also try other optimized approaches, such as solvent vapor annealing and adding additives, and the Detailed photovoltaic parameters are shown in Table S9. We find that a D-A weight ratio of 1:1 in chloroform and thermal annealing at 120°C for ZITI-C and ZITI-N and 100°C for ZITI-S are the best device fabrication conditions. As shown in Figure 2C and Table 1, J71:ZITI-S-based devices show relatively low PCEs of $8.86 \pm 0.18\%$ with a V_{oc} of 0.812 ± 0.004 V, a J_{sc} of 17.18 ± 0.38 mA cm^{-2}, and fill factor (FF) of $63.51 \pm 0.87\%$; J71:ZITI-C and J71:ZITI-N-based devices exhibit high PCEs of $13.02 \pm 0.13\%$ and $13.47 \pm 0.12\%$ with V_{oc}s of 0.851 ± 0.006, 0.873 ± 0.005 V, J_{sc}s of 21.28 ± 0.26, 21.73 ± 0.33 mA cm^{-2}, and FF of $72.03 \pm 0.79\%$, $70.96 \pm 0.88\%$, respectively. The corresponding histogram of PCE counts for 25 individual devices is displayed in Figure S7. Also, ZITI-N possesses an
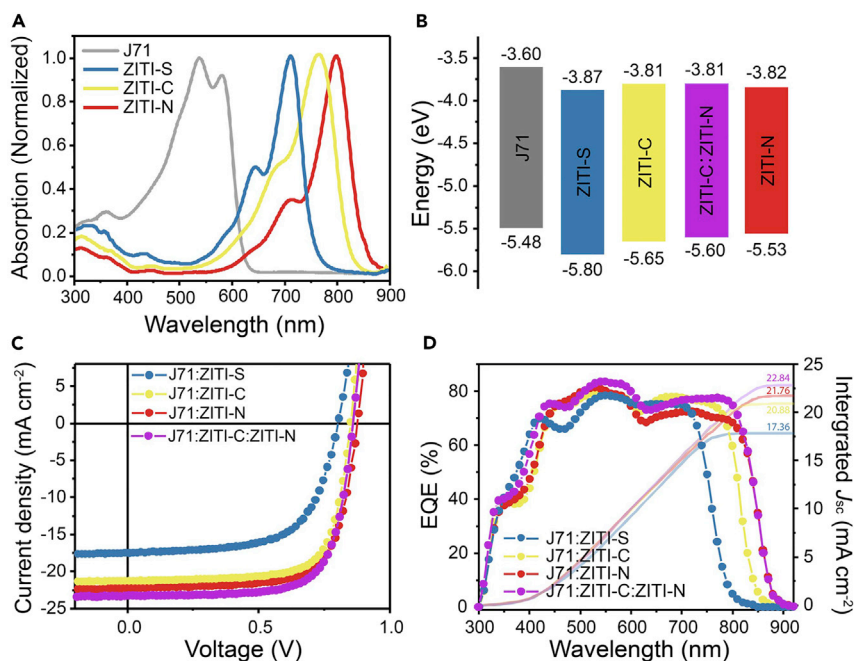
Figure 2. PV Performance of J71:ZITI-X-Based OSCs

(A) Normalized UV-vis-NIR absorption spectra of ZITI-X and J71 in thin films.

(B) Energy diagram of donor and acceptor materials.

(C) Characteristic J-V curves.

(D) The corresponding EQE curves of J71:ZITI-X-based devices.

excellent compatibility with commercially available polymer donors (See Table S11). Despite the lowest optical bandgap of ZITI-N, the J71:ZITI-N blend gives the highest V_{oc} with the lowest E_{loss} of 0.53 eV than J71:ZITI-S and J71:ZITI-C blends with E_{loss}s of 0.80 and 0.62 eV, which can be correlated to HOMO energy levels. The J_{sc}s are confirmed by EQE measurements (see Figure 2D). ZITI-N-based devices show a slightly lower EQE_{max} of 72.50% than ZITI-S- and ZITI-C-based ones with EQE_{max} of 74.35% and 78.01% in the NIR region, suggesting that the driving force (HOMO energy offsets) corresponds to carrier extraction. Such observation inspires us to blend ZITI-C and ZITI-N together, to balance the driving force and absorption (Liu et al., 2018b; Zhang et al., 2018c). We fabricated the ternary OSCs and optimized the acceptor ratios and thickness (See Tables S4 and S7). ZITI-C/N (1:1) HOMO energy level can be tuned to −5.60 eV (see Figure 2B), leading to a slightly increased HOMO offset (hole transfer driving force). As expected, a PCE_{avg} of 14.05 ± 0.21% with a V_{oc} of 0.857 ± 0.004 V, a J_{sc} of 23.01 ± 0.24 mA cm^{-2}, and an FF of 71.72 ± 0.98% is obtained (see Figure 2C). The increased J_{sc} accounts for the improved PCE. Accordingly, a higher NIR EQE_{max} of 77.07% is obtained, suggesting improved charge separation. Moreover, the thick-film device is very important to meet the needs of future roll-to-roll mass production and lay the foundation for the commercial applications. We tried to fabricate the J71:ZITI-C:ZITI-N-based ternary devices with the different thickness (Table S12). The PCE still maintains over 12% when the thickness of the active layer increases to 200 nm.

To investigate the charge transport property in the blend films, the electron and hole mobilities are measured by using the space-charge-limited-current method (see Figure S4 and Table S5). The J71:ZITI-S device shows electron and hole mobilities of 1.54 × 10^{-4} and 2.75 × 10^{-4} cm^2 V^{-1} s^{-1}. J71:ZITI-C, J71:ZITI-N, and J71:ZITI-C:ZITI-N devices show the electron/hole mobilities of 1.86 × 10^{-4}/3.83 × 10^{-4}, 2.12 × 10^{-4}/2.69 × 10^{-4}, and 2.24 × 10^{-4}/2.82 × 10^{-4} cm^2 V^{-1} s^{-1}, respectively. To investigate the carrier recombination under the short-circuit condition, we measured the current density at different light intensities (see Figure S9). All devices displayed the same relationship of $J_{sc} = P^{0.95}$, indicating the weak bimolecular recombination for these blends. The dependence of V_{oc} on the light intensity was measured resulting in slopes of 1.23, 1.32, 1.15, and 1.18 kT/q for J71:ZITI-S, J71:ZITI-C, J71:ZITI-N, and J71:ZITI-C:ZITI-N devices, respectively, implying low trap-assisted recombination.

Acceptors	V_{oc} (V)	bJ_{sc} (mA cm^{-2})	FF (%)	PCE (%)	E_g^{opt} (eV)	E_{loss} (eV)
ZITI-S	0.811 (0.812 ± 0.004)	17.39 (17.18 ± 0.38)	64.62 (63.51 ± 0.87)	9.12 (8.86 ± 0.18)	1.61	0.80
ZITI-C	0.851 (0.851 ± 0.006)	21.30 (21.28 ± 0.26)	72.76 (72.03 ± 0.79)	13.18 (13.02 ± 0.13)	1.47	0.62
ZITI-N	0.876 (0.873 ± 0.005)	21.78 (21.73 ± 0.33)	72.00 (70.96 ± 0.88)	13.68 (13.47 ± 0.12)	1.41	0.53
ZITI-C :ZITI-N	0.859 (0.857 ± 0.004)	23.05 (23.01 ± 0.24)	72.51 (71.72 ± 0.98)	14.36 (14.05 ± 0.21)	1.41	0.55

Table 1. Photovoltaic Parameters of J71:ZITI-X-Based Devices
Average values with standard deviation were obtained from 25 devices.

Thin-film morphology of neat materials and BHJ blends were investigated using grazing incidence wide-angle X-ray diffraction (GIWAXS) and resonant soft X-ray scattering (RSoXS) (see Figure 3). J71 shows a face-on orientation with (100) at 0.29 Å^{-1} and a π-π stacking at 1.69 Å^{-1}. ZITI-X series in neat films show similar molecular stacking of face-on orientations. The (100) peak is located at ∼0.32 Å^{-1} and the π-π stacking peak is located at 1.72, 1.85, and 1.70 Å^{-1} for ZITI-S, ZITI-C, and ZITI-N, respectively. Thus, detailed change in bridge heteroatoms can affect the π-π stacking of conjugated backbone. BHJ thin films show similar diffraction features for all these samples, except slight changes in the π-π stacking position, containing both J71 and ZITI-X structure information. RSoXS at 285.2 eV photon energy was used to investigate the phase separation of BHJ thin films. J71:ZITI-S shows a scattering hump at 0.014 Å^{-1}, indicating a phase separation of 45 nm. J71:ZITI-C and J71:ZITI-N show quite similar scattering feature, with a scattering hump around 0.01 Å^{-1}, indicating a phase separation of 63 nm. J71:ZITI-C:ZITI-N ternary blends retains a similar phase separation. Such morphology information is in good agreement with atomic force microscopy (AFM) and transmission electron microscopy (TEM) characterizations. The AFM under typing mode and TEM are utilized to detect the morphologies of blend films. As shown in Figure S6, J71:ZITI-S, J71:ZITI-C, J71:ZITI-N, and J71:ZITI-C:ZITI-N blends display very uniform and smooth surface with root-mean-square (RMS) roughnesses of 0.73, 0.86, 1.19, and 0.94 nm, respectively. TEM images are quite consistent with AFM in the changes of the fibrillar structures and self-aggregation of the blend films.

Energy Loss Analysis

To understand the origin of V_{oc} difference, study on the energy loss pathways in J71:ZITI-X blends were conducted with Fourier-transform photocurrent spectroscopy, external quantum efficiency (FTPS-EQE), electroluminescence (EL), and electroluminescence quantum efficiency (EQE$_{EL}$) measurements. The total energy loss E_{loss} can be attributed to two parts: energy loss due to charge generation ($\Delta E_2 = E_g - E_{CT}$) and energy loss due to charge recombination ($E_{CT} - qV_{oc}$) that can be divided into the radiative (ΔE_1) and non-radiative (ΔE_3) recombinations.[4,5] The E_{CT} of each blend systems can be calculated by fitting sub-gap absorption of the corresponding FTPS-EQE curves using the following equation (Vandewal et al., 2010):

$$EQE_{PV}(E) = \frac{f}{E\sqrt{4\pi\lambda kT}}e^{\frac{-E_{CT}+\lambda-E}{4\lambda kT}}$$

where $EQE_{PV}(E)$ is the photovoltaic external quantum efficiency, k is the Boltzmann constant, T is the absolute temperature (300 K in this work), and λ is the reorganization energy and f can be viewed as the interaction strength between donor and acceptor in the blends. E_{loss} can be calculated according to the following equation (Qian et al., 2018; Vandewal et al., 2010):

$$E_{loss} = E_{gap} - qV_{oc} = (E_{gap} - E_{CT}) + \left[-kT\ln\left(\frac{J_{sc}h^3c^2}{fq2\pi(E_{CT}-\lambda)}\right)\right] + \left[-\frac{kT}{q}\ln(EQE_{EL})\right] = \Delta E_2 + \Delta E_1 + \Delta E_3$$

where h is the Plank constant, q is the elementary charge, and c is the speed of light.

Figure 4A shows the normalized EL spectra of the devices based on pure materials and blends. The J71:ZITI-S blend shows a single EL emission peak at 1,010 nm, which is assigned to the emission from the sub-gap charge transfer (CT) state. The strong CT state density can be a result of large energy level
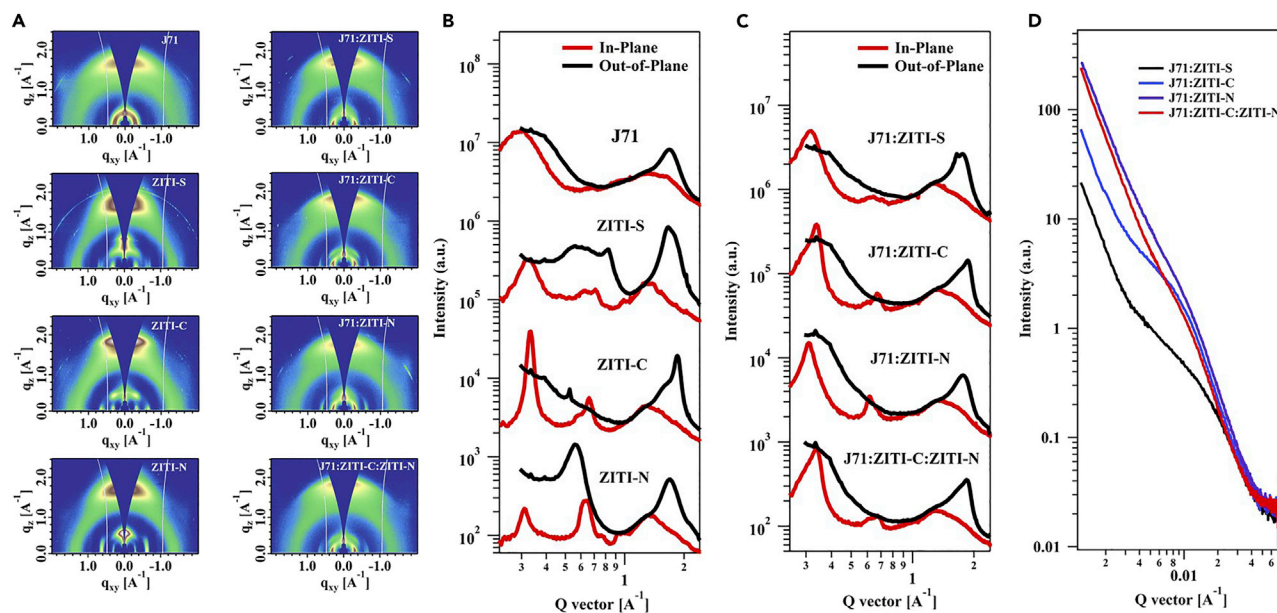
Figure 3. Morphology Investigations
(A) GIWAXS 2D patterns for ZITI-X pristine films and J71:ZITI-X blend films.
(B and C) The corresponding line-cuts of GIWAXS patterns of neat films and BHJ films.
(D) RSoXS profiles for J71:ZITI-X blend films.

offsets (HOMO and LUMO); thus, the charge generation energy loss is strong. For the J71:ZITI-C blend, a weak and new CT emission peak also appears at around 1,010 nm together with another main emission band at around 906 nm assigned to ZITI-C; thus, such blend has a low CT state density that can be quickly filled and then to generate ZITI-C emission. The J71:ZITI-N blend only shows EL from ZITI-N, without noticeable CT states emission. Thus, quite low charge generation loss is presented owing to the small energy level offset. The FTPS-EQE curves (see Figure 4B) are used to obtain CT energy through the above-mentioned equation. The CT energy for J71:ZITI-S blend is 1.36 eV, resulting in an E_g-E_{CT} energy offset (ΔE_2: 0.30 eV). In contrast, both J71:ZITI-C and J71:ZITI-N blends show higher E_{CT} (1.45 V for J71:ZITI-C and 1.44 eV for J71:ZITI-N) leading to much smaller E_g-E_{CT} offsets (ΔE_2: 0.10 eV for J71:ZITI-C and 0.07 eV for J71:ZITI-N). Because the V_{oc} of OSCs is directly restricted by the energy of the CT state, J71:ZITI-C and J71:ZITI-N blends with high CT energies could achieve higher V_{oc} compared with that of the J71:ZITI-S blend. The energy losses due to radiative recombination (ΔE_1) of charge carriers are calculated using the fitted parameters from the FTPS-EQE spectra, and the losses due to the non-radiative recombination (ΔE_3) can be quantified by measuring the EQE$_{EL}$. As ΔE_1 is unavoidable for all kinds of solar cells, it is important to maximize EQE$_{EL}$ to minimize ΔE_3. As shown in Figure 4C and Table S6, the emission efficiency of J71:ZITI-N blend is 8.16×10^{-4}%, one order of magnitude higher than those of the other two blends, 2.54×10^{-5}% (J71:ZITI-S) and 4.39×10^{-5}% (J71:ZITI-C), which represents significantly decreased non-radiative recombination losses (0.30 eV) compared with other blends (0.39 eV for J71:ZITI-S and 0.38 eV for J71:ZITI-C). Therefore, we attribute the highest V_{oc} of J71:ZITI-N blend to the smallest E_g-E_{CT} energy offset and the suppressed non-radiative recombination losses (Figure 4D). For the driving force that leads to the charge generation ($\Delta E_2 = E_g$-E_{CT}) or in other words the energy loss generated during the exciton dissociation process, the J71:ZITI-S blend has the largest value of 0.30 eV due to large energy offsets in both HOMO and LUMO. ZITI-C and ZITI-N have quite similar LUMO energy levels, and thus the difference in driving force comes from the energy offsets from HOMO side. Thus, manipulating the HOMO energy level is an important route in mitigating the energy loss in BHJ blends. The energy loss analysis of ternary OSCs are shown in Figure S5 and Table S6. In the ternary blends, whose chemical similarity makes molecular alloy possible, make a useful platform to fine-tune frontier energy levels. Such a strategy can effectively manipulate the detailed energy loss and driving force, two factors that interactively affect V_{oc} and J_{sc}. Such an optimization yields improved device performances with a maximized PCE of 14.36%, a success of physical understanding in improving efficiency of using existing materials.
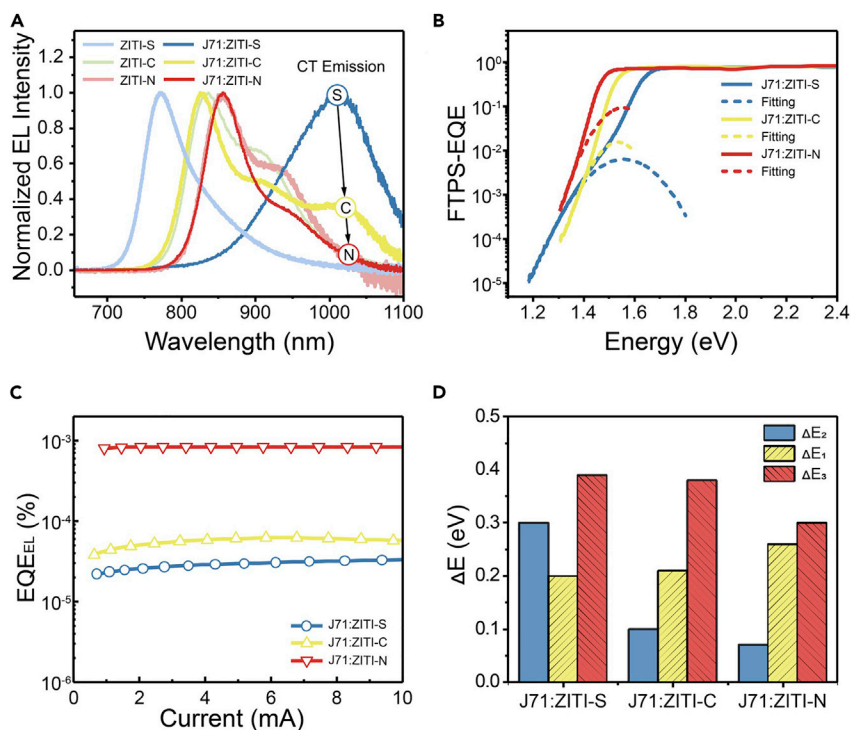
Figure 4. Energy Loss Analysis
(A) Electroluminescence spectra of devices based on the pristine NFAs and blended films.
(B and C) FTPS-EQE and EQE_{EL} of the blended devices.
(D) The comparison of ΔE_1, ΔE_2, and ΔE_3 of J71:ZITI-X-based devices.

Hole-Transfer Kinetics and Driving Force Correlation

To quantitatively assess the HOMO energy offset, or driving force on photoinduced hole transfer process, we performed femtosecond (fs) transient absorption (TA) spectroscopy to directly probe the photo-induced hole transfer dynamics in J71:ZITI-S, J71:ZITI-C, J71:ZITI-N, and J71:ZITI-C:ZITI-N blend films (see Figure 5). The steady-state absorption peaks for different acceptors and donors are well separated in spectral domain; therefore, both spectral and temporal characteristics of charge transfer dynamics can be extracted. To investigate hole transfer, the excitation wavelength of 750 nm was selected here to excite only acceptors. The color plot of fs TA spectra of J71:ZITI-S film after 750-nm excitation are shown in Figure 5A and a few representative TA spectra at indicated delay times in Figure 5B with TA spectrum of neat ZITI-S film (gray circles) also shown for comparison. The bleach peaks at ~650 and 730 nm appear in both neat ZITI-S and J71:ZITI-S films, corresponding to the ground state bleach and the stimulated emission of the lowest energy transition (S_1) in ZITI-S due to photoexcitation. With the decay of ZITI-S bleach peak at 630–760 nm, a few new bleach peaks at 550–620 nm appear in the TA spectrum of J71:ZITI-S film. These peaks at 550–620 nm match very well with the absorption features of J71 films. The bleach decay process of photoexcited ZITI-S (630–760 nm) agrees well with the rise process of the J71 ground state bleach (550–620 nm), confirming photoexcited hole transfer from ZITI-S to J71. The hole transfer in J71:ZITI-C, J71:ZITI-N, and J71:ZITI-C:ZITI-N blend films are also observed as shown in Figure S8 in spite of smaller HOMO energy offsets. The ground state bleach of J71 in J71:ZITI-S, J71:ZITI-C, and J71:ZITI-N blend films rise with a half-time of ~3.2, 4.7, and 20 ps, respectively, corresponding to the hole transfer lifetime. This trend of hole transfer rate agrees with the value of HOMO offsets. Thus, a higher driving force is critical in ensuring efficient carrier extraction from NFA acceptors to enhance J_{sc}. The high J_{sc} obtained from J71:ZITI-N blends is attributed to the extended absorption. Blending ZITI-C with ZITI-N recovers the hole-transfer lifetime to 7.0 ps. Such an operation better balances the light absorption and extraction efficiency, yielding the highest J_{sc} among BHJ devices. We also investigated the photo-induced electron transfer process by exciting the J71 donor and probing its excited state absorption at 1,175 nm. The decay kinetics of the J71 excited state in different blend films are shown in Figure 5D, which shows that electron
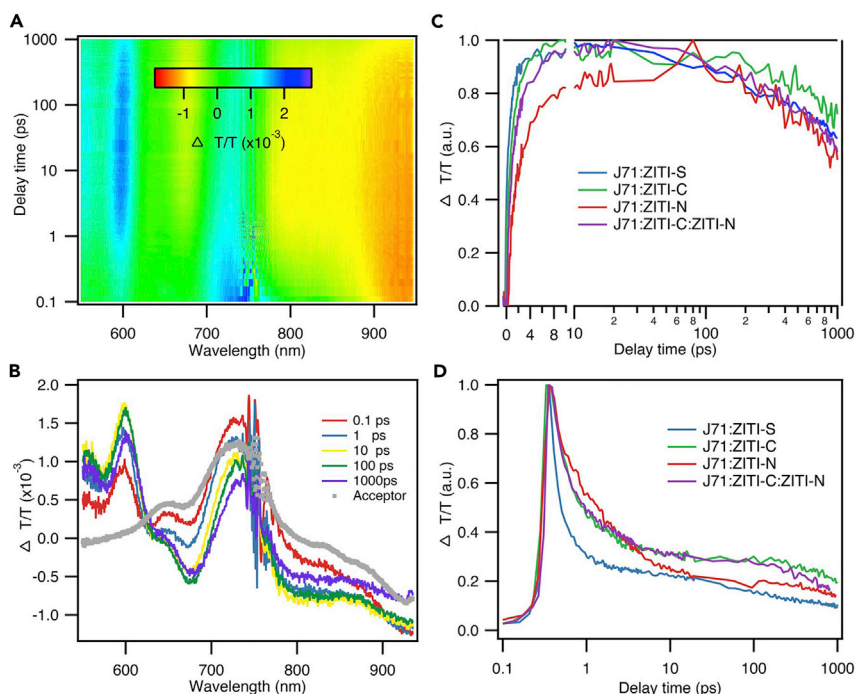
Figure 5. Transient Absorption Analysis

(A) Color plot of fs Transient absorption spectra of J71:ZITI-S blend film under 750 nm excitation with a fluence below 10 $\mu J/cm^2$.

(B) Representative fs Transient absorption spectra of J71:ZITI-S blend film at indicated delay times; Gray dots: TA spectrum of neat ZITI-S film at 1 ps excited by 750 nm.

(C) TA kinetics of J71:ZITI-S, J71:ZITI-C, J71:ZITI-N, and J71:ZITI-C:ZITI-N blend films showing hole transfer process.

(D) TA kinetics of excited state absorption (1175 nm) of J71:ZITI-S, J71:ZITI-C, J71:ZITI-N, and J71:ZITI-C:ZITI-N blend films showing electron transfer process.

transfers in all blend films are very efficient and are shorter than 1 ps. Thus, hole-transfer process is the major barrier in generating device current.

Driving Force, Energy Loss, Charge Extraction, and Absorption Manipulation

The previous discussions reveal the importance of manipulating frontier energy levels to better balance driving force, energy loss, and charge extraction. We make J71:ZITI-C:ZITI-N ternary blends of more blending ratios to establish a correlation. Thin film absorption and internal quantum efficiency (IQE) were first explored. As shown in Figure 6A, the J71:ZITI-N blend film shows the stronger absorbance of 0.654 at the maximum absorption of 793 nm than J71:ZITI-C, 0.466 at 750 nm. However, as shown in IQE curves (see Figure 6B), the J71:ZITI-N blend delivers a weaker IQE response of 79.47% (793 nm) compared with that of the J71:ZITI-C blend, 83.05% (750 nm). Thus, despite the largest spectral overlap with sunlight of ZITI-N that is essential to get a large J_{sc}, the J71:ZITI-N blend gives only a comparable J_{sc} of 21.73 ± 0.33 mA cm^{-2} as that of ZITI-C, 21.28 ± 0.26 mA cm^{-2}. Such result clearly demonstrates the complex inter-connection between material bandgap and system driving force in generating current. A simple 1:1 mixing, although low in peak absorption (790 nm), elevates the driving force of hole transfer, giving rise to a high IQE value of 86.05%. And thus a higher J_{sc} of 23.01 ± 0.24 mA cm^{-2} is obtained. A more detailed correlation can be seen in ternary blends of different compositions. As expected, high ZITI-N loading could reduce the effective HOMO energy level in the mixture, and thus a low energy loss and a high V_{oc} can be obtained, as seen from the monotonic increase in Figure 6C. In J_{sc} spectrum, a higher ZITI-N loading should linearly increase J_{sc} if only absorption is considered. However, high J_{sc} is seen in mixtures, with the highest value at 1:1 ratio. Such result unequivocally reveals the importance of driving force in helping charge extraction, ensuring high device J_{sc}. And thus the maximum efficiency is obtained when ZITI-C:ZITI-N = 1:1 (Figure 6D). Thus, the detailed balance among driving force, energy loss, charge extraction, and light absorption should be carefully manipulated in high efficiency OPV devices. Interestingly, by changing the donor J71 to
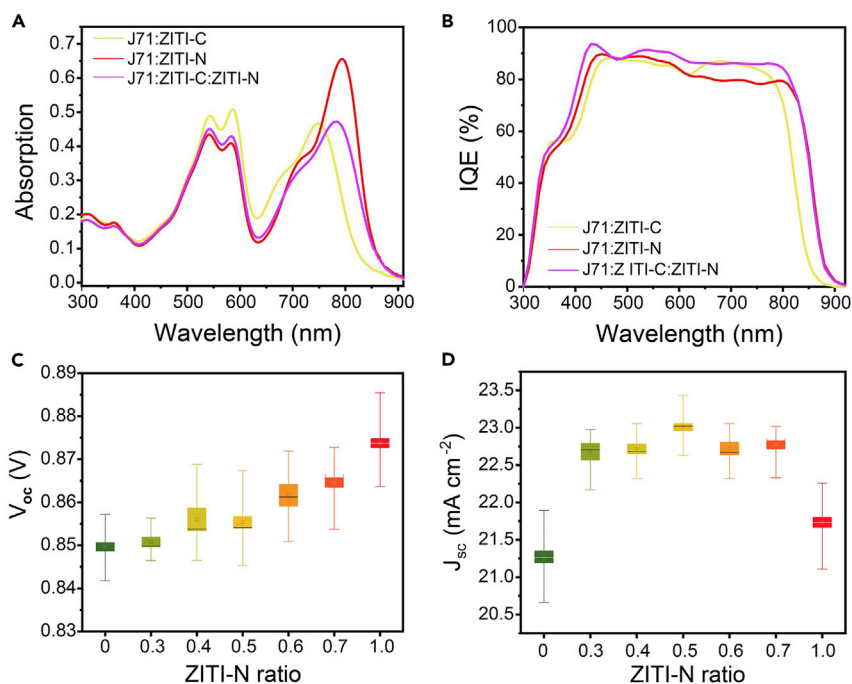
Figure 6. Current and Voltage Balance Analysis

(A and B) BHJ blends absorption profiles and internal quantum efficiency of J71:ZITI-C:ZITI-N binary and ternary blends.
(C and D) V_{oc} and J_{sc} dependence on ZITI-N ratio in ternary blends.

PBDB-TF, the ternary OSCs-based PBDB-TF:ZITI-C:ZITI-N achieve a higher PCE of 13.85% with simultaneously elevated J_{sc} and FF than the binary OSCs (Table S10).

Conclusions

To conclude, we achieved a panoramic understanding of the relationship between driving force and OSCs performance with a new family of NIR electron acceptors, ZITI-S, ZITI-C, and ZITI-N, possessing high structural similarity. Among the three acceptors, ZITI-N exhibits the highest HOMO energy level and the lowest optical bandgap of 1.41 eV with an absorption onset at 879 nm. When blended with the wide-bandgap polymer donor, J71:ZITI-N-based devices deliver the highest PCE_{avg} of 13.47 $\pm$ 0.12% at the smallest E_{loss} of 0.53 eV than those of J71:ZITI-S- and J71:ZITI-C-based devices with PCE_{avg}s of 8.86 $\pm$ 0.18% and 13.02 $\pm$ 0.13% and E_{loss}s of 0.80 and 0.62 eV, respectively. Furthermore, by combining ZITI-C and ZITI-N acceptors, a higher PCE_{avg} of 14.05 $\pm$ 0.21% with an improved J_{sc} of 23.01 $\pm$ 0.24 mA cm^{-2} is achieved, which can be ascribed to the slightly increased driving force according to the detailed study on the energy loss channels. The fs-TA spectroscopy investigation indicates that the J71:ZITI-N blend with the lowest HOMO offset shows the slowest hole transfer rate. We observed that the CT emissions gradually decreased and finally disappeared from J71:ZITI-S, J71:ZITI-C to J71:ZITI-N blends, which means that, when the active layers have both optimized morphology and excellent absorption, by narrowing HOMO offset between donor and acceptor materials, the superiority of NFAs can be fully realized. Investigations by implementing PL quenching and EL experiments provide valuable information on the efficiency of charge separation and the magnitude of driving force, which may accelerate the donor:acceptor screening and relieve the workload from the tedious device fabrication. Moreover, with the ideal research models based on J71 and ZITI-X, we unambiguously reveal that a meticulous control of HOMO offset is critical to approaching the efficiency limit in NFA OSCs.

Limitations of Study

In our research system, when we investigate the relationship between HOMO offset and the efficiency for charge separation, we can exclude the impact originating from the blend morphology because of the high structural similarity of ZITI-X NIR acceptors. However, the morphology impact should be carefully considered in other systems.

METHODS

All methods can be found in the accompanying Transparent Methods supplemental file.

SUPPLEMENTAL INFORMATION

Supplemental Information can be found online at https://doi.org/10.1016/j.isci.2019.08.038.

AUTHOR CONTRIBUTIONS

J.Z., W.L., and M.Z. contributed equally to this work. J.Z. fabricated and optimized the devices; W.L. and S.X. synthesized the ZITI-S, ZITI-C, and ZITI-N; F.L. performed the morphology analysis and analyzed the whole data; Y.L. performed the PL, EL, and FTPS-EQE experiments, which were supervised by F.Z. G.Z. performed the transient absorption spectroscopy, which was supervised by H.Z. X.Z. conceived and directed the project. All authors discussed the results and substantially contributed to the preparation of the manuscript.

DECLARATION OF INTERESTS

The authors declare no competing interests.

REFERENCES

Cha, H., Tan, C.-H., Wu, J., Dong, Y., Zhang, W., Chen, H., Rajaram, S., Narayan, K.S., McCulloch, I., and Durrant, J.R. (2018). An analysis of the factors determining the efficiency of photocurrent generation in polymer: nonfullerene acceptor solar cells. Adv. Energy Mater 8, 1801537.

Chen, S., Wang, Y., Zhang, L., Zhao, J., Chen, Y., Zhu, D., Yao, H., Zhang, G., Ma, W., Friend, R.H., and Chow, P.C.Y. (2018). Efficient nonfullerene organic solar cells with small driving forces for both hole and electron transfer. Adv. Mater. 30, 1804215.

Cheng, P., Li, G., Zhan, X., and Yang, Y. (2018). Next-generation organic photovoltaics based on non-fullerene acceptors. Nat. Photon. 12, 131–142.

Cui, Y., Yao, H., Zhang, J., Zhang, T., Wang, Y., Hong, L., Xian, K., Xu, B., Zhang, S., Peng, J., et al. (2019). Over 16% efficiency organic photovoltaic cells enabled by a chlorinated acceptor with increased open-circuit voltages. Nat. Commun. 10, 2515.

Fei, Z., Fei, Z., Eisner, F.D., Jiao, X., Azzouzi, M., Röhr, J.A., Han, Y., Shahid, M., Chesman, A.S.R., Easton, C.D., et al. (2018). An alkylated indacenodithieno[3,2-b]thiophene-based nonfullerene acceptor with high crystallinity exhibiting single junction solar cell efficiencies greater than 13% with low voltage losses. Adv. Mater. 30, 1705209.

Hou, J., Inganas, O., Friend, R.H., and Gao, F. (2018). Organic solar cells based on non-fullerene acceptors. Nat. Mater. 17, 119–128.

Kan, B., Feng, H., Wan, X., Liu, F., Ke, X., Wang, Y., Wang, Y., Zhang, H., Li, C., Hou, J., and Chen, Y. (2017). Small-molecule acceptor based on the heptacyclic benzodi(cyclopentadithiophene) unit for highly efficient nonfullerene organic solar cells. J. Am. Chem. Soc. 139, 4929–4934.

Kan, B., Zhang, J., Liu, F., Wan, X., Li, C., Ke, X., Wang, Y., Feng, H., Zhang, Y., Long, G., et al. (2018). Fine-tuning the energy levels of a nonfullerene small-molecule acceptor to achieve a high short-circuit current and a power conversion efficiency over 12% in organic solar cells. Adv. Mater. 30, 1704904.

Kang, H., Kim, G., Kim, J., Kwon, S., Kim, H., and Lee, K. (2016). Bulk-heterojunction organic solar cells: Five core technologies for their commercialization. Adv. Mater. 28, 7821–7861.

Li, T., Dai, S., Ke, Z., Yang, L., Wang, J., Yan, C., Ma, W., and Zhan, X. (2018a). Fused tris(thienothiophene)-based electron acceptor with strong near-infrared absorption for high-performance as-cast solar cells. Adv. Mater. 30, 1705969.

Li, W., Ye, L., Li, S., Yao, H., Ade, H., and Hou, J. (2018b). A high-efficiency organic solar cell enabled by the strong intramolecular electron push-pull effect of the nonfullerene acceptor. Adv. Mater. 30, 1707170.

Li, Y., Zhong, L., Gautam, B., Bin, H., Lin, J., Wu, F., Zhang, Z., Jiang, Z., Zhang, Z., Gundogdu, K., et al. (2017a). A near-infrared non-fullerene electron acceptor for high performance polymer solar cells. Energy Environ. Sci. *10*, 1610–1620.

Li, Y., Lin, J.-D., Che, X., Qu, Y., Liu, F., Liao, L.-S., and Forrest, S.R. (2017b). High efficiency near-infrared and semitransparent non-fullerene acceptor organic photovoltaic cells. J. Am. Chem. Soc. *139*, 17114–17119.

Lin, Y., Wang, J., Zhang, Z.G., Bai, H., Li, Y., Zhu, D., and Zhan, X. (2015). An electron acceptor challenging fullerenes for efficient polymer solar cells. Adv. Mater. *27*, 1170–1174.

Liu, F., Zhou, Z., Zhang, C., Zhang, J., Hu, Q., Vergote, T., Liu, F., Russell, T.P., and Zhu, X. (2017). Efficient semitransparent solar cells with high NIR responsiveness enabled by a small-bandgap electron acceptor. Adv. Mater. *29*, 1606574.

Liu, J., Chen, S., Qian, D., Gautam, B., Yang, G., Zhao, J., Bergqvist, J., Zhang, F., Ma, W., Ade, H., et al. (2016). Fast charge separation in a non-fullerene organic solar cell with a small driving force. Nat. Energy *1*, 16089.

Liu, T., Luo, Z., Chen, Y., Yang, T., Xiao, Y., Zhang, G., Ma, R., Lu, X., Zhan, C., Zhang, M., et al. (2019). A nonfullerene acceptor with 1000 nm absorption edge enables ternary organic solar cells with improved optical and morphological properties and efficiencies over 15%. Energy Environ. Sci. https://doi.org/10.1039/C9EE01030K.

Liu, W., Zhang, J., Zhou, Z., Zhang, D., Zhang, Y., Xu, S., and Zhu, X. (2018a). Design of a new fused-ring electron acceptor with excellent compatibility to wide-bandgap polymer donors for high-performance organic photovoltaics. Adv. Mater. *30*, 1800403.

Liu, T., Luo, Z., Fan, Q., Zhang, G., Zhang, L., Gao, W., Guo, X., Ma, W., Zhang, M., Yang, C., et al. (2018b). Use of two structurally similar small molecular acceptors enabling ternary organic solar cells with high efficiencies and fill factors. Energy Environ. Sci. *11*, 3275–3282.

Lu, L., Zheng, T., Wu, Q., Schneider, A.M., Zhao, D., and Yu, L. (2015). Recent advances in bulk heterojunction polymer solar cells. Chem. Rev. *115*, 12666–12731.

Menke, S.M., Ran, N.A., Bazan, G.C., and Friend, R.H. (2018). Understanding energy loss in organic solar cells: toward a new efficiency regime. Joule *2*, 25–35.

Nian, L., Kan, Y., Wang, H., Gao, K., Xu, B., Rong, Q., Wang, R., Wang, J., Liu, F., Chen, J., et al. (2018). Ternary non-fullerene polymer solar cells with 13.51% efficiency and a record-high fill factor of 78.13%. Energy Environ. Sci. *11*, 3392–3399.

Qian, D., Zheng, Z., Yao, H., Tress, W., Hopper, T.R., Chen, S., Li, S., Liu, J., Chen, S., Zhang, J., et al. (2018). Design rules for minimizing voltage losses in high-efficiency organic solar cells. Nat. Mater. *17*, 703–709.

Sun, J., Ma, X., Zhang, Z., Yu, J., Zhou, J., Yin, X., Yang, L., Geng, R., Zhu, R., Zhang, F., and Tang, W. (2018). Dithieno[3,2-*b*:2′,3′-*d*]pyrrol fused nonfullerene acceptors enabling over 13% efficiency for organic solar cells. Adv. Mater. *30*, 1707150.

Vandewal, K., Tvingstedt, K., Gadisa, A., Inganas, O., and Manca, J.V. (2009). On the origin of the open-circuit voltage of polymer-fullerene solar cells. Nat. Mater. *8*, 904–909.

Vandewal, K., Tvingstedt, K., Gadisa, A., Inganäs, O., and Manca, J.V. (2010). Relating the open-circuit voltage to interface molecular properties of donor: acceptor bulk heterojunction solar cells. Phys. Rev. B *81*, 125204.

Wadsworth, A., Moser, M., Marks, A., Little, M.S., Gasparini, N., Brabec, C.J., Baran, D., and McCulloch, I. (2019). Critical review of the molecular design progress in non-fullerene electron acceptors towards commercially viable organic solar cells. Chem. Soc. Rev. *48*, 1596–1625.

Xie, Y., Yang, F., Li, Y., Uddin, M.A., Bi, P., Fan, B., Cai, Y., Hao, X., Woo, H.Y., Li, W., et al. (2018). Morphology control enables efficient ternary organic solar cells. Adv. Mater. *30*, 1803045.

Xu, S., Zhou, Z., Liu, W., Zhang, Z., Liu, F., Yan, H., and Zhu, X. (2017). A twisted thieno[3,4-*b*] thiophene-based electron acceptor featuring a 14-π-electron indenoindene core for high-performance organic photovoltaics. Adv. Mater. *29*, 1704510.

Yamaguchi, S., and Tamao, K. (2015). A key role of orbital interaction in the main group element-containing π-electron systems. Chem. Lett. *34*, 2–7.

Yan, C., Barlow, S., Wang, Z., Yan, H., Jen, A.K.-Y., Marder, S.R., and Zhan, X. (2018). Non-fullerene acceptors for organic solar cells. Nat. Mater. Rev. *3*, 18003.

Yao, H., Chen, Y., Qin, Y., Yu, R., Cui, Y., Yang, B., Li, S., Zhang, K., and Hou, J. (2016). Design and synthesis of a low bandgap small molecule acceptor for efficient polymer solar cells. Adv. Mater. *28*, 8283–8287.

Yao, J., Kirchartz, T., Vezie, M.S., Faist, M.A., Gong, W., He, Z., Wu, H., Troughton, J., Watson, T., Bryant, D., et al. (2015). Quantifying losses in open-circuit voltage in solution-processable solar cells. Phys. Rev. Appl. *4*, 014020.

Yu, G., Gao, J., Hummelen, J.C., Wudl, F., and Heeger, A.J. (1995). Polymer photovoltaic cells: enhanced efficiencies via a network of internal donor-acceptor heterojunctions. Science *270*, 1789–1791.

Yu, R., Yao, H., Hong, L., Xu, Y., Gao, B., Zhu, J., Zu, Y., and Hou, J. (2018). Enhancing the photovoltaic performance of nonfullerene acceptors via conjugated rotatable end groups. Adv. Energy Mater *8*, 1802131.

Yu, Z., Liu, Z.X., Chen, F.X., Qin, R., Lau, T.K., Yin, J.L., Kong, X., Lu, X., Shi, M., Li, C.Z., and Chen, H. (2019). Simple non-fused electron acceptors for efficient and stable organic solar cells. Nat. Commun. *10*, 2152.

Yuan, J., Zhang, Y., Zhou, L., Zhang, G., Yip, H.-L., Lau, T.-K., Lu, X., Zhu, C., Peng, H., Johnson, P.A., et al. (2019). Single-junction organic solar cell with over 15% efficiency using fused-ring acceptor with electron-deficient core. Joule *3*, 1140–1151.

Zhang, G., Zhao, J., Chow, P.C.Y., Jiang, K., Zhang, J., Zhu, Z., Zhang, J., Huang, F., and Yan, H. (2018a). Nonfullerene acceptor molecules for bulk heterojunction organic solar cells. Chem. Rev. *118*, 3447–3507.

Zhang, H., Yao, H., Hou, J., Zhu, J., Zhang, J., Li, W., Yu, R., Gao, B., Zhang, S., and Hou, J. (2018b). Over 14% efficiency in polymer solar cells enabled by a chlorinated polymer donor. Adv. Mater. *30*, 1800613.

Zhang, J., Liu, W., Chen, S., Xu, S., Yang, C., and Zhu, X. (2018c). One-pot synthesis of electron-acceptor composite enables efficient fullerene-free ternary organic solar cells. J. Mater. Chem. A *6*, 22519–22525.

Zhao, W., Li, S., Yao, H., Zhang, S., Zhang, Y., Yang, B., and Hou, J. (2017). Molecular optimization enables over 13% efficiency in organic solar cells. J. Am. Chem. Soc. *139*, 7148–7151.

Zhou, Z., Xu, S., Song, J., Jin, Y., Yue, Q., Qian, Y., Liu, F., Zhang, F., and Zhu, X. (2018). High-efficiency small-molecule ternary solar cells with a hierarchical morphology enabled by synergizing fullerene and non-fullerene acceptors. Nat. Energy *3*, 952–959.

Supplemental Information

Revealing the Critical Role of the HOMO

Alignment on Maximizing Current Extraction

and Suppressing Energy Loss in Organic Solar Cells

Jianyun Zhang, Wenrui Liu, Ming Zhang, Yanfeng Liu, Guanqing Zhou, Shengjie Xu, Fengling Zhang, Haiming Zhu, Feng Liu, and Xiaozhang Zhu

Supplemental Information

Revealing the Critical Role of the HOMO Alignment on Maximize Current Extraction and Suppress Energy Loss in Organic Solar Cells

Jianyun Zhang,[1,2,7] Wenrui Liu,[1,2,7] Ming Zhang,[4,7] Yanfeng Liu,[3] Guanqing Zhou,[4] Shengjie Xu,[1,*] Fengling Zhang,[3] Haiming Zhu,[5] Feng Liu,[4,*] and Xiaozhang Zhu[1,2,6,*]

[1]Beijing National Laboratory for Molecular Sciences, CAS Key Laboratory of Organic Solids, Institute of Chemistry, Chinese Academy of Sciences, Beijing 100190, China

[2]School of Chemical Sciences, University of Chinese Academy of Sciences, Beijing 100190, China

[3]Department of Physics, Chemistry and Biology (IFM), Linköping University, Linköping SE-581 83, Sweden

[4]School of Chemistry and Chemical Engineering, and Center for Advanced Electronic Materials and Devices, Shanghai Jiao Tong University, Shanghai 200240, China

[5]Department of Chemistry, Zhejiang University, Hangzhou 310027, China

[6]Lead Contact

[7]These authors contributed equally: Jianyun Zhang, Wenrui Liu, Ming Zhang

*Correspondence: xushengjie@iccas.ac.cn (S.X.), *fengliu82@sjtu.edu.cn (F.L.), *xzzhu@iccas.ac.cn (X.Z.)

1. Transport Method

Materials

The J71 was purchased from Solarmer Inc.; all materials were used in the condition they were received, without further purification. The molecular weight of polymer donor J71 is 18.573 kDa.

AFM

Atomic force microscopy (AFM) images of the thin films were obtained on a NanoscopeIIIa AFM (Digital Instruments) operating platform in tapping mode. The samples were prepared by spinning coated the active layers on the PEDOT:PSS layer.

TEM

Transmission electron microscopy (TEM) observation was performed on JEOL 2200 FS at 160 kV accelerating voltage. The samples for electron microscopy were prepared by dissolving the PEDOT:PSS layer using water and transferring the floating active layer to the TEM grids.

Scattering Characterization

The GIWAXS characterization of the thin films was performed at the Advanced Light Source (Lawrence Berkeley National Laboratory) on beamline 7.3.3. Samples were prepared under device conditions on the Si/PEDOT:PSS substrates. R-SoXS was performed at beamline 11.0.1.2 (ALS, LBNL). Samples were prepared under device conditions on the Si/PEDOT:PSS substrates, then placed in water and transferred to a silicon nitride window that obtained from CleanSiN.

PL Measurement

The pumping light source used to excite the samples was a green laser (532 nm), with a power of 10 mW. The PL spectra were recorded with an Andor spectrometer (Shamrock sr-303i-B), which was coupled with a Newton electron multiplying CCD (EMCCD) detector.

EL Measurement

An external current/voltage source was employed to provide an external electric field to the pristine and blended solar cells. The EL emissions were recorded with an Andor spectrometer.

FTPS-EQE Measurement

The FTPS-EQE was measured with a Vertex 70 from Bruker Optics, which was equipped with a quartz tungsten halogen lamp, quartz beam-splitter and external detector option. A low-noise current amplifier (SR570) was used to amplify the photocurrent produced under illumination of the solar cells, with light modulated by the Fourier transform infrared spectroscope (FTIR). The output voltage of the current amplifier was fed back into the external detector port of the FTIR to use the FTIR software to collect the photocurrent spectra.

EQE$_{EL}$ Measurement.

The EQE$_{EL}$ was recorded with an in-house-built system comprising a Hamamatsu silicon photodiode 1010B, Keithley 2400 source meter (for supplying voltages and recording injected currents), and Keithley 485 picoammeter (for measuring the emitted light intensity).

Transient Absorption Spectroscopy

For femtosecond transient absorption spectroscopy, the fundamental output from Yb:KGW laser (1030 nm, 220 fs Gaussian fit, 100 kHz, Light Conversion Ltd) was separated to two light beam. One was introduced to NOPA (ORPHEUS-N, Light Conversion Ltd) to produce a certain wavelength for pump beam (here we use 550 and 750 nm, 30 fs pulse duration), the other was focused onto a YAG plate to generate white light continuum as probe beam. The pump and probe overlapped on the sample at a small angle less than 10°. The transmitted probe light from sample was collected by a linear CCD array.

Device Development and Testing.

The devices were developed with a conventional structure of ITO/PEDOT:PSS/active layer/PDINO/Al. The ITO-coated glass substrates were cleaned with sequential ultrasonication in a soap-deionized water mixture, deionized water, acetone, and isopropanol. The washed substrates were further treated with oxygen plasma for 10 min to eliminate any remaining organic components. A thin layer (ca. 30 nm) of PEDOT:PSS (Clevios P VP 4083) was first spin-coated on the ITO substrates at 3,000 rpm and baked at 150 °C for 5 min under ambient conditions. The substrates were then transferred into a nitrogen-filled glove box. Subsequently, the active layers were spin coated from chloroform solution with the same optimal donor/acceptor (D/A) weight ratios of 1:1 for both J71: ZITI-S (or ZITI-C, ZITI-N, ZITI-C:ZITI-N) blends with a total concentration of 19 mg/mL. J71: ZITI-S blends was treated with thermal annealing at 100 °C, J71:ZITI-C, J71:ZITI-N and J71:ZITI-C:ZITI-N blends were treated with thermal annealing at 120 °C for 10 min. Then PDINO as the electron transporting layer was spin-coated on the active layer by 3000 rpm from alcohol solution. In the final stage, the substrates were pumped down in high vacuum, and aluminum (100 nm) was thermally evaporated onto the active

layer. Shadow masks were used to define the OSC active area (0.05 cm^2) of the devices. The current density–voltage (*J*–*V*) characteristics of the PV devices were measured under N$_2$ conditions using a Keithley 2400 source meter. An AAA grade solar simulator, with an air mass (AM) 1.5 global filter operated at 100 mW cm^{-2}, was used to simulate the AM 1.5G solar irradiation. The illumination intensity was corrected by using a standard monocrystalline silicon reference cell, with a protective KG5 filter calibrated by the National Renewable Energy Laboratory (NREL). The *J-V* curves were measured along the forward scan direction from −0.2 V to 1.5 V or the reverse scan direction from 1.5 V to −0.2 V, yielding identical results. The scan speed and dwell times were fixed at 0.015 V s^{-1} and 20 ms, respectively. The EQE was calculated using certified incident photon to current conversion efficiency (IPCE) equipment from Enlitech (Taiwan).

SCLC Mobility Measurements.

SCLCs were tested in electron-only devices configured with the ITO/ZnO/active layer/Al and hole-only devices configured with the ITO/PEDOT:PSS/active layer/MoO$_3$/Au. The mobilities were determined by fitting the dark-field current to the model of a single carrier SCLC current with field dependent mobility, which is described as

$$J = \frac{9\varepsilon_0\varepsilon_r\mu_0 V^2}{8L^3}$$

where *J* represents the current, μ_0 represents the zero-field mobility, ε_0 represents the permittivity of free space, ε_r represents the relative permittivity of the material, *V* represents the effective voltage, and *L* represents the thickness of the active layer. From the plot of $J^{1/2}$ vs *V*, the hole and electron mobilities can be deduced.

2. Synthetic Procedures
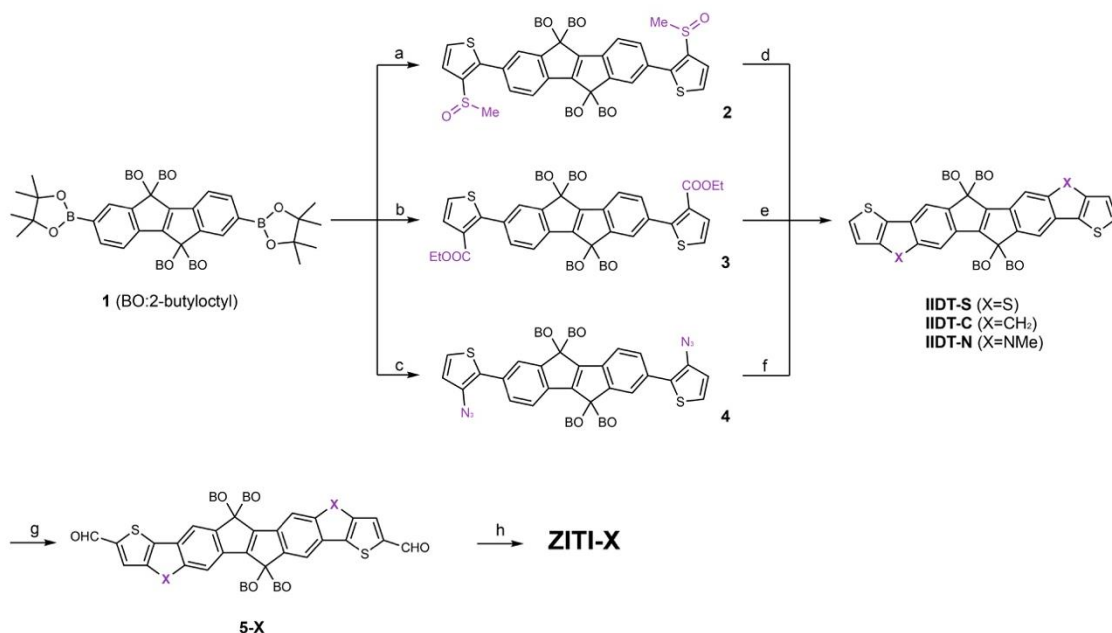
Supplementary Scheme 1 | Synthesis of ZITI-X NFAs. Reagents and conditions: **a**, 2-Bromo-3-(methylsulfinyl)thiophene, Pd(PPh₃)₄, aqueous Na₂CO₃, dioxane. **b**, Ethyl 2-bromothiophene-3-carboxylate, Pd(PPh₃)₄, aqueous Na₂CO₃, dioxane. **c**, (i) 2,3-Dibromothiophene, Pd(PPh₃)₄, THF. (ii) *n*-BuLi, Tos-N₃, THF; **d**, Eaton's reagent, pyridine. **e**, (i) KOH, ethanol; (ii) Oxalyl chloride, CH₂Cl₂, DMF. (iii) AlCl₃, CH₂Cl₂. **f**, (i) *o*-dichlorobenzene, 160 °C. (ii) NaH, CH₃I, DMF. **g**, POCl₃, DMF. **h**, INCN-2F, pyridine, CHCl₃.

Compound 2. Compound **1** (565 mg, 0.5 mmol) and 2-bromo-3-(methylsulfinyl)thiophene (338 mg, 1.5 mmol, 3 equiv.) were added to 19 mL of a 1:2 *v/v* mixture of aqueous Na₂CO₃ (2.0 M) and dioxanes under argon. The reaction mixture was purged with argon for 10 minutes and then Pd(PPh₃)₄ catalyst (58 mg, 0.05 mmol, 0.1 equiv.) was added. The reaction solution was stirred at 95 °C overnight under argon atmosphere and then was poured into ethyl acetate. The organic layer was washed with water and brine, and was dried over MgSO₄. The solvent was removed under reduced pressure. The resulting orange solid was purified on a silica-gel column chromatography to give 340 mg of compound **2** as a yellow solid (58%). ^{1}H NMR (300 MHz, CDCl₃): δ 7.63 (d, ^3J = 5.4 Hz, 2H), 7.62 (s, 2H), 7.43 (d, ^3J = 5.4 Hz, 2H), 7.40 (m, 4H), 2.75 (s, 6H), 2.04 (s, 8H), 1.20–0.60 (m, 92H); ^{13}C NMR (100 MHz, CDCl₃): δ 156.8, 145.4, 145.3, 145.2, 141.1, 139.6, 139.6, 132.0, 128.6, 127.8, 127.7, 127.5, 126.1, 126.0, 125.9, 125.6, 124.9, 124.8, 124.1, 120.3, 54.3, 44.9, 42.9, 42.2, 42.1, 35.0, 34.8, 34.7, 34.6, 34.5, 33.8, 33.7, 31.9, 31.8, 29.9, 29.8, 29.7, 28.1, 28.0, 27.9, 27.9, 27.8, 27.7, 25.9, 25.8, 25.7, 25.6, 23.1, 23.0, 22.7, 22.6, 14.2, 14.1, 14.0; HRMS (MALDI-TOF) calcd for C₇₄H₁₁₇O₂S₄ [M+H]⁺: 1165.7931, found, 1165.7949.

Compound IDTT-S. Compound **2** (210 mg, 0.18mmol) was stirred with Eaton's reagent (8 mL) at room temperature in the dark for 3 days. The mixture was poured into ice-water, extracted with chloroform and the organic phase was dried with MgSO₄, the solvent was removed by reduced pressure and the crude product was dried in vacuum, which was followed to be redissolved in pyridine (10 mL) and then the mixture was refluxed overnight. After the mixture was cooled to room temperature, extracted with chloroform and diluted hydrochloride acid, the separated organic phase was dried over MgSO₄, and solvent was removed by reduced pressure. The crude was purified by column chromatography on silica gel column chromatography to afford a pale yellow solid **IDTT-S** (60 mg, 30 %). ^{1}H NMR (400 MHz, CDCl₃): δ 7.79 (s, 2H), 7.75 (s, 2H), 7.44 (d, ^3J = 5.2 Hz, 2H),

7.30 (d, ^3J = 4.8 Hz, 2H), 2.12 (m, 8H), 1.20–0.50 (m, 92H); ^{13}C NMR (100 MHz, CDCl$_3$): δ 156.0, 155.9, 155.8, 153.3, 153.2, 153.1, 141.6, 138.2, 138.1, 137.3, 137.2, 135.3, 129.2, 126.6, 120.4, 115.7, 115.6, 115.5, 114.5, 53.6, 53.4, 43.2, 43.0, 42.9, 42.8, 35.2, 35.0, 34.6, 34.5, 34.4, 34.3, 33.6, 31.9, 31.8, 29.9, 29.8, 29.7, 29.6, 28.5, 28.4, 27.7, 27.6, 26.2, 26.1, 25.28, 25.2, 25.1, 25.0, 23.1, 22.9, 22.8, 22.6, 14.1, 14.0, 13.9, 13.8; HRMS (MALDI-TOF) calcd for C$_{72}$H$_{108}$S$_4$ [M]$^+$: 1100.7328, found, 1100.7308.

Compound 4. Compound **1** (843 mg, 0.81 mmol) was dissolved in dry tetrahydrofuran, then slowly added a solution of 2,3-dibromothiophen (588 mg, 2.43 mmol, 3 equiv.) in tetrahydrofuran, Pd(PPh$_3$)$_4$ (94 mg, 0.081 mmol) was then added. The reaction solution was refluxed overnight at 95 °C. The organic layer was washed with water and brine, and was dried over MgSO$_4$. The solvent was removed under reduced pressure. The resulting orange solid was purified on a silica-gel column chromatography to give 530 mg yellow solid (54%). ^{1}H NMR (400 MHz, CDCl$_3$): δ 7.66 (s, 2H), 7.57 (d, ^3J = 7.6 Hz, 2H), 7.37 (d, ^3J = 7.6 Hz, 2H), 7.25 (m, 2H), 7.06 (t, ^3J = 5.6 Hz, 2H), 2.05 (s, 8H), 1.20–0.60 (m, 92H); ^{13}C NMR (100 MHz, CDCl$_3$): δ 156.5, 155.9, 140.5, 139.4, 131.8, 128.5, 127.3, 124.3, 123.9, 119.7, 106.9, 54.2, 42.9, 35.0, 34.9, 34.8, 34.6, 33.7, 31.9, 29.9, 29.7, 28.2, 27.8, 26.0, 25.6, 23.2, 23.0, 22.7, 14.1, 14.0; HRMS (MALDI-TOF) calcd for C$_{72}$H$_{110}$Br$_2$S$_2$ [M]$^+$: 1196.6410, found, 1196.6409. A solution of this yellow solid (500 mg, 0.42 mmol) in 20 mL of dry ether was added dropwise with stirring at -78 °C to n-butyllithium (0.63 mL, 1.6 M in n-hexane). The reaction mixture was stirred for 45 min at -78 °C, after which an ethereal solution of *p*-toluenesulfonyl azide (206 mg, 1.05 mmol) was added dropwise. After the addition was complete, the resulting mixture was stirred for 5 h at -78 °C. When the temperature had reached -10 °C, the resulting triazene salt was rapidly filtered off and washed with dry ether. The solid material was then suspended in 150 mL of ether and treated with a solution of 222 mg (0.82 mmol) of tetrasodium pyrophosphate in 10 mL of water. After the mixture was stirred overnight at 5 °C, the organic layer was separated, and the aqueous solution was extracted twice with ether, and was dried over MgSO$_4$. The solvent was removed under reduced pressure and used for the next step without further purification.

Compound IDTT-N. Compound **4** was stirred for 8 h at 160 °C in *o*-dichlorobenzene. The solvent was removed under reduced pressure. The resulting solid was purified on a silica-gel column chromatography to give 70 mg yellow solid (16%). ^{1}H NMR (400 MHz, CDCl$_3$): δ 8.08 (s, 2H), 7.65 (s, 2H), 7.33 (s, 2H), 7.27 (m, 2H), 7.05 (t, ^3J = 3.6 Hz, 2H), 2.05 (s, 8H), 1.25–0.50 (m, 92H); ^{13}C NMR (100 MHz, CDCl$_3$): δ 155.5, 148.0, 142.5, 140.8, 137.0, 125.1, 119.1, 118.8, 113.3, 111.3, 102.8, 53.0, 43.4, 35.2, 35.0, 34.2, 33.5, 32.0, 31.9, 31.8, 29.9, 29.8, 29.7, 28.4, 26.1, 23.1, 22.9, 22.6, 14.1, 14.0, 13.9; HRMS (MALDI-TOF) calcd for C$_{72}$H$_{110}$N$_2$S$_2$ [M]$^+$: 1066.8105, found, 1066.8104. A solution of this yellow solid (53 mg, 0.05 mmol) in 5 mL of dry DMF was added dropwise with stirring at 0 °C to NaH (10 mg, 0.25 mmol). The resulting mixture was stirred for 1 h at 25 °C, CH$_3$I (70 mg, 0.5 mmol) was then added into the mixture. The reaction solution was stirred overnight. The organic layer was washed with water and brine, and was dried over MgSO$_4$. The solvent was removed under reduced pressure. The resulting solid was purified on a silica-gel column chromatography to give 45 mg of **IDTT-N** as a yellow solid (80%).^{1}H NMR (400 MHz, CDCl$_3$): δ 7.66 (s, 2H), 7.29 (d, ^3J = 4.8 Hz, 2H), 7.24 (s, 2H), 7.06 (t, ^3J = 2.4 Hz, 2H), 3.91 (s, 6H), 2.15 (m, 8H), 1.15–0.50 (m, 92H); ^{13}C NMR (100 MHz, CDCl$_3$): δ 155.6, 147.4, 145.3, 141.6, 136.8, 124.8, 118.7, 116.5, 113.3, 110.0, 100.6, 53.1, 13.3, 35.2, 35.0, 34.4, 33.5, 32.1, 31.9, 31.8, 31.3, 30.0, 29.9, 29.7, 29.6, 28.5, 27.6, 26.2, 26.1, 25.1, 23.2, 23.1, 23.0, 22.6, 14.1, 14.0, 13.8; HRMS (MALDI-TOF) calcd for C$_{74}$H$_{114}$N$_2$S$_2$ [M]$^+$: 1094.8418, found, 1094.8418.

Compound 5-S. POCl$_3$ (22 µL, 0.23 mmol) was slowly added into 5 mL dry DMF under N2, after stirring at RT for 30 min. Compound **IDTT-S** (50 mg, 0.045 mmol) was added and the mixture was stirred at 70 °C overnight. The solvent was evaporated, and the residue was purified on a silica-gel column to give compound **5-S** (50 mg, 96%).^{1}H NMR (400 MHz, CDCl$_3$): δ 10.01 (s, 2H), 7.99 (s, 2H), 7.91 (s, 2H), 7.82 (s, 2H), 2.16 (s, 8H), 1.25–0.50 (m, 92H); ^{13}C NMR (100 MHz, CDCl$_3$): δ 181.9, 181.8, 156.5, 156.4, 156.3, 153.1, 153.0, 152.9, 143.5, 143.0, 141.7, 139.1, 136.6, 136.5, 136.4, 128.7, 127.6, 127.5, 115.8, 115.7, 115.6, 113.8, 52.8, 52.4, 42.0, 41.8, 41.7, 41.6, 34.2, 34.1,

33.9, 33.6, 33.5, 33.4, 33.3, 32.7, 30.9, 30.8, 30.7, 28.8, 28.6, 28.5, 27.5, 27.4, 26.6, 26.5, 26.4, 25.1, 25.0, 24.2, 24.1, 24.0, 23.9, 22.0, 21.8, 21.7, 21.6, 13.1, 13.0, 12.9, 12.8, 12.7; HRMS (MALDI-TOF) calcd for $C_{74}H_{109}O_2S_4$ [M+H]$^+$: 1157.7305, found, 1157.7202.

Compound 5-N. The synthesis method is similar to **5-S**. The starting material **IDTT-S** was replaced by **IDTT-N**. The final product was obtained as a dark-green solid (93% yield). ^{1}H NMR (400 MHz, CDCl$_3$): δ 9.94 (s, 2H), 7.76 (s, 2H), 7.71 (s, 2H), 7.29 (s, 2H), 3.94 (s, 6H), 2.17 (s, 8H), 1.30–0.50 (m, 92H); ^{13}C NMR (100 MHz, CDCl$_3$): δ 183.03, 182.9, 157.5, 157.4, 148.7, 148.6, 148.5, 144.7, 143.9, 142.2, 139.6, 139.5, 125.6, 118.3, 118.2, 118.1, 117.8, 114.8, 114.7, 101.1, 53.4, 43.2, 43.1, 35.3, 35.2, 35.0, 34.5, 34.4, 34.3, 33.7, 33.6, 32.0, 31.8, 31.7, 31.2, 29.9, 29.8, 29.7, 29.6, 28.6, 28.5, 27.5, 27.4, 26.3, 26.2, 25.1, 25.0, 24.9, 23.1, 22.9, 22.8, 22.6, 14.1, 14.0, 13.9, 13.8, 13.7; HRMS (MALDI-TOF) calcd for $C_{76}H_{114}N_2O_2S_2$ [M]$^+$: 1150.8316, found, 1150.8319.

Compound ZITI-S. INCN-2F (51 mg, 0.22 mmol) and compound **5-S** (50 mg, 0.043 mmol) were added to a solvent mixture of chloroform (10 mL) and pyridine (5 drops). The reaction was placed in an oil bath at 75 °C and was stirred for 18 hours. The mixture was directly purified on a silica-gel column chromatography using chloroform as eluent to give 45 mg of **ZITI-S** as black solid (66%). ^{1}H NMR (300 MHz, CDCl$_3$): δ 9.03 (s, 2H), 8.58 (m, 2H), 8.15 (s, 2H), 8.05 (s, 2H), 7.76 (s, 2H), 7.74 (t, ^3J = 7.5 Hz, 2H), 2.18 (s, 8H), 1.20–0.50 (m, 92H); HRMS (MALDI-TOF) calcd for $C_{100}H_{116}F_4N_4O_2S_2$ [M]$^+$: 1580.7575, found, 1580.7599.

Compound ZITI-C. The synthesis method is similar to **ZITI-S**. The starting material **5-S** was replaced by **5-CH₂**. The final product was obtained as a dark-green solid (61% yield). ^{1}H NMR (400 MHz, CDCl$_3$): δ 8.96 (s, 2H), 8.55 (m, 2H), 7.92 (s, 2H), 7.79 (s, 2H), 7.68 (t, ^3J = 7.6 Hz, 2H), 7.57 (s, 2H), 3.88 (s, 4H), 2.13 (s, 8H), 1.30–0.50 (m, 92H); ^{13}C NMR (150 MHz, CDCl$_3$): δ 186.2, 165.2, 159.2, 158.9, 157.2, 155.5, 155.4, 153.7, 153.6, 148.6, 142.8, 140.1, 138.8, 136.8, 134.8, 134.6, 120.2, 117.5, 117.1, 115.2, 115.0, 114.8, 114.7, 112.7, 112.5, 68.8, 54.4, 43.3, 43.1, 35.4, 35.1, 34.8, 34.1, 33.8, 32.2, 32.1, 32.0, 30.0, 29.9, 28.6, 27.9, 27.8, 26.3, 26.2, 25.5, 25.4, 23.3, 23.0, 22.9, 22.8, 14.2, 14.2, 14.0; HRMS (MALDI-TOF) calcd for $C_{100}H_{116}F_4N_4O_2S_2$ [M]$^+$: 1544.8470, found, 1544.8479.

Compound ZITI-N. The synthesis method is similar to **ZITI-S**. The starting material **5-S** was replaced by **5-NMe**. The final product was obtained as a dark-green solid (60% yield). ^{1}H NMR (400 MHz, CDCl$_3$): δ 8.99 (s, 2H), 8.54 (m, 2H), 7.92 (s, 2H), 7.82 (s, 2H), 7.69 (t, ^3J = 7.6 Hz, 2H), 7.28 (s, 2H), 3.95 (s, 6H), 2.19 (m, 8H), 1.20–0.50 (m, 92H); ^{13}C NMR (100 MHz, CDCl$_3$): δ 185.8, 159.6, 158.9, 155.7, 153.0, 149.4, 146.7, 146.3, 142.0, 138.8, 138.1, 136.8, 134.6, 124.0, 120.3, 118.8, 115.8, 115.0, 114.8, 114.7, 112.5, 112.3, 101.4, 68.0, 53.5, 43.1, 35.1, 34.9, 34.5, 33.8, 32.0, 31.8, 31.7, 31.4, 29.9, 29.8, 29.7, 29.6, 28.5, 27.4, 26.1, 25.0, 23.1, 22.9, 22.8, 22.6, 22.6, 14.1, 14.0, 13.9, 13.8; HRMS (MALDI-TOF) calcd for $C_{100}H_{118}F_4N_6O_2S_2$ [M]$^+$: 1574.8688, found, 1574.8691.

Abbreviations:

ITIC:
2,2'-[[6,6,12,12-tetrakis(4-hexylphenyl)-6,12-dihydrodithieno[2,3-*d*:2',3'-*d'*]-*s*-indaceno[1,2-*b*:5,6-*b*']dithiophene-2,8-diyl]bis[methylidyne(3-*oxo*-1*H*-indene-2,1(3*H*)-diylidene)]]bis[propanedinitrile]

BT-IC:
(4,4,10,10-tetrakis(4-hexylphenyl)-5,11-(2-ethylhexyloxy)-4,10-dihydrodithienyl[1,2-*b*:4,5-*b*']benzodithiophene-2,7-diyl)bis[methylidyne(3-*oxo*-1*H*-indene-2,1(3*H*)-diylidene)]]bis[propanedinitrile]

BDT-IC:
2,2'-[[4,4,10,10-Tetrakis(4-hexylphenyl)-4,10-dihydrothieno[3',2':4,5]cyclopenta[1,2-*b*]thieno[2'',3'':3',4']cyclopenta[1',2':4,5]thieno[2,3-*f*][1]benzothiophene-2,8-diyl] bis[methylidyne(3-*oxo*-1*H*-indene-2,1(3*H*)-diylidene)]]bis[propanedinitrile]

NITI:
2,2'-[[6,6'-[5,5,10,10-tetrakis(2-hexyldecyl)-5,10-dihydroindeno[2,1-*a*]indene-2,7-diyl)bis(2-octylthieno[3,4-*b*]thiophene]-4,4'-diyl]bis[methylidyne(5,6-difluoro-3-*oxo*-1*H*-indene-2,1(3*H*)-diylidene)]]bis[propanedinitrile]

ZITI-S:
2,2'-[[6,6,13,13-tetrakis(2-butyloctyl)-6,13-dihydroindeno[1,2:2',1']indeno[5,6-*d*:5',6'-*d'*]dithieno[3,2-*b*:3',2'-*b*']dithiophene-2,9-diyl]bis[methylidyne(5,6-difluoro-3-*oxo*-1*H*-indene-2,1(3*H*)-diylidene)]]bis[malononitrile]

ZITI-C:
2,2'-[[6,6,13,13-tetrakis(2-butyloctyl)-6,13-dihydro-*s*-indaceno[5,6:6',5']-*s*-indaceno[1,2-*b*:1',2'-*b*']dithiophene-2,9-diyl]bis[methylidyne(5,6-difluoro-3-*oxo*-1*H*-indene-2,1(3*H*)-diylidene)]]bis[malononitrile]

ZITI-N:
2,2'-[[6,6,13,13-tetrakis(2-butyloctyl)-4,11-dimethyl-4,6,11,13-tetrahydropentaleno[2,1-*f*:5,4-*f'*]dithieno[3,2-*b*:3',2'-*b*']diindole-2,9-diyl]bis[methylidyne(5,6-difluoro-3-*oxo*-1*H*-indene-2,1(3*H*)-diylidene)]]bis[malononitrile]

IIDT-S:
6,6,13,13-tetrakis(2-butyloctyl)-6,13-dihydro-*s*-indaceno[5,6:6',5']-*s*-indaceno[1,2-*b*:1',2'-b']dithiophene

IIDT-C:
6,6,13,13-tetrakis(2-butyloctyl)-6,13-dihydroindeno[1,2:2',1']indeno[5,6-*d*:5',6'-*d'*]dithieno[3,2-*b*:3',2'-*b*']dithiophene

IIDT-N:
6,6,13,13-tetrakis(2-butyloctyl)-4,11-dimethyl-4,6,11,13-tetrahydropentaleno[2,1-*f*:5,4-*f'*]dithieno[3,2-*b*:3',2'-*b*']diindole

3. Supporting Figures and Tables

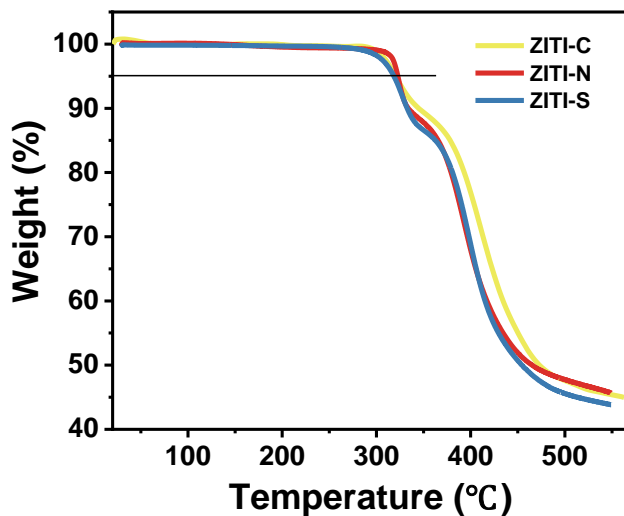**Figure S1. Thermal gravimetric analysis curves of ZITI-S, ZITI-C, and ZITI-N.**
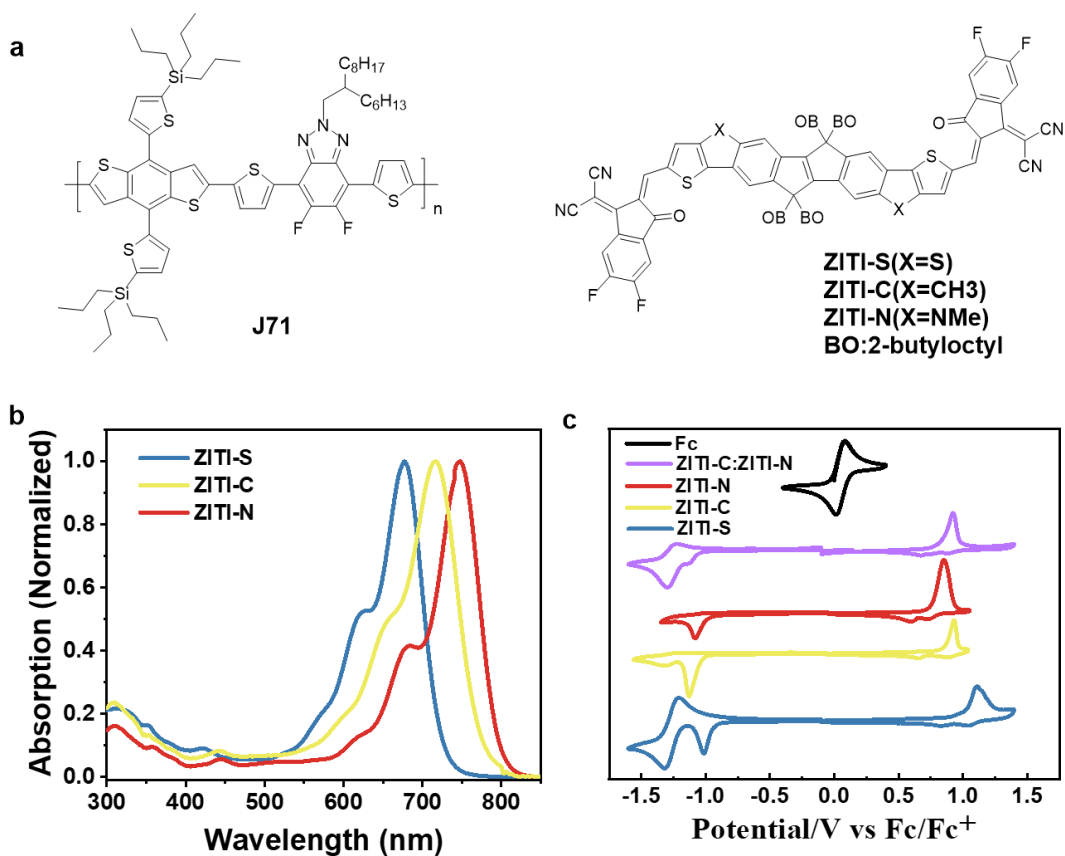
Figure S2. Photoelectric properties of ZITI-X. (a) The structure of the polymer and acceptors. (b) UV-vis-NIR absorption spectra of ZITI-S, ZITI-C, and ZITI-N in chloroform. (c) Cyclic voltammogram of ZITI-S, ZITI-C, ZITI-N, and ZITI-C:ZITI-N film in diluted CH_3CN solution with a scan rate of 100 mV s^{-1}.
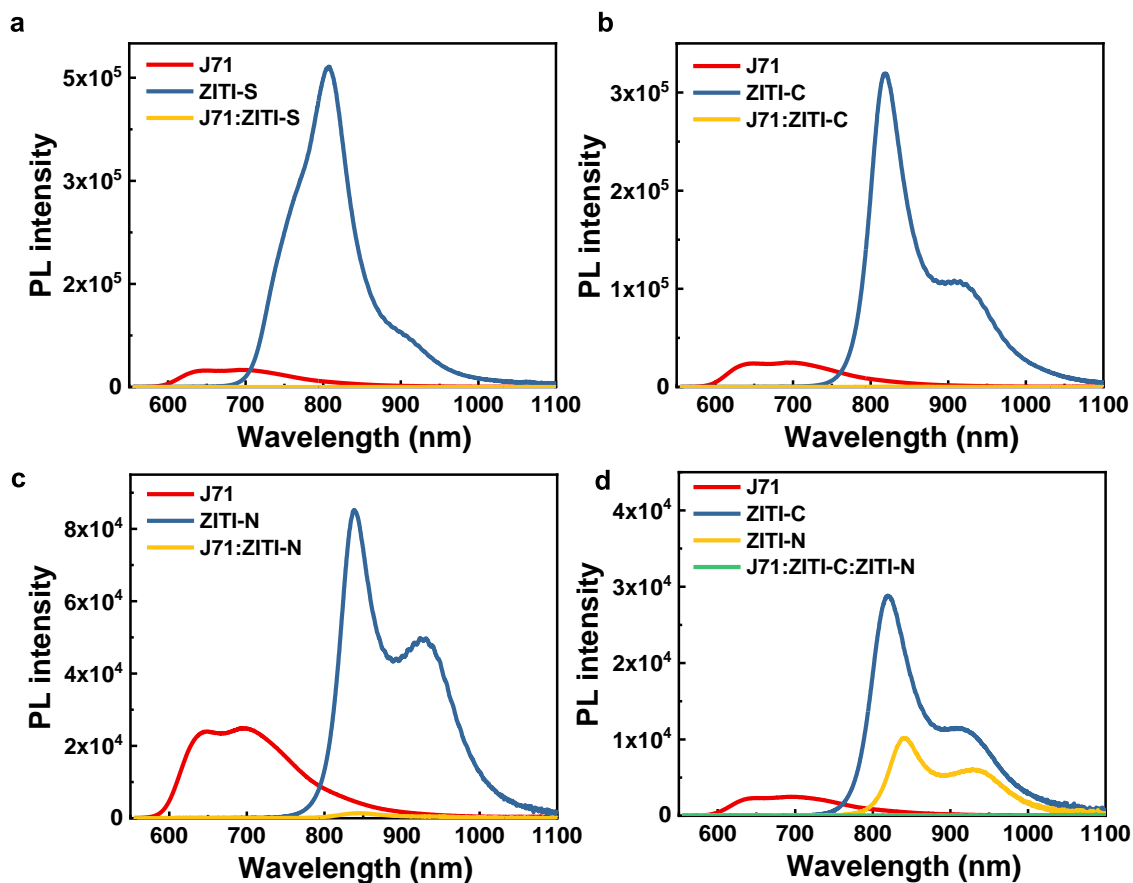
Figure S3. PL quenching. PL spectra of (a) the pristine donor J71, ZITI-S, and blended films, (b) the pristine donor J71, ZITI-C, and blended films, (c) the pristine donor J71, ZITI-N, and blended films, (d) the pristine donor J71, ZITI-C, ZITI-N, and blended films. For the PL measurements, the intensities are corrected by their absorptions at the excitation wavelength (532 nm).
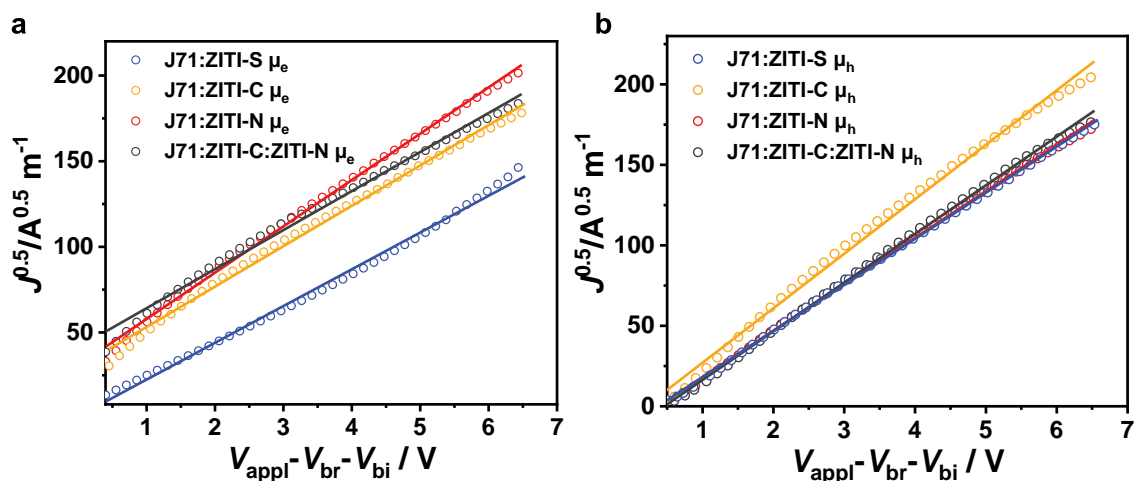
Figure S4. $J^{0.5}$ vs V plots of (a) electron-only diode and (b) hole-only diode in J71:ZITI-S, J71:ZITI-C, J71:ZITI-N, and J71:ZITI-C:ZITI-N blends.
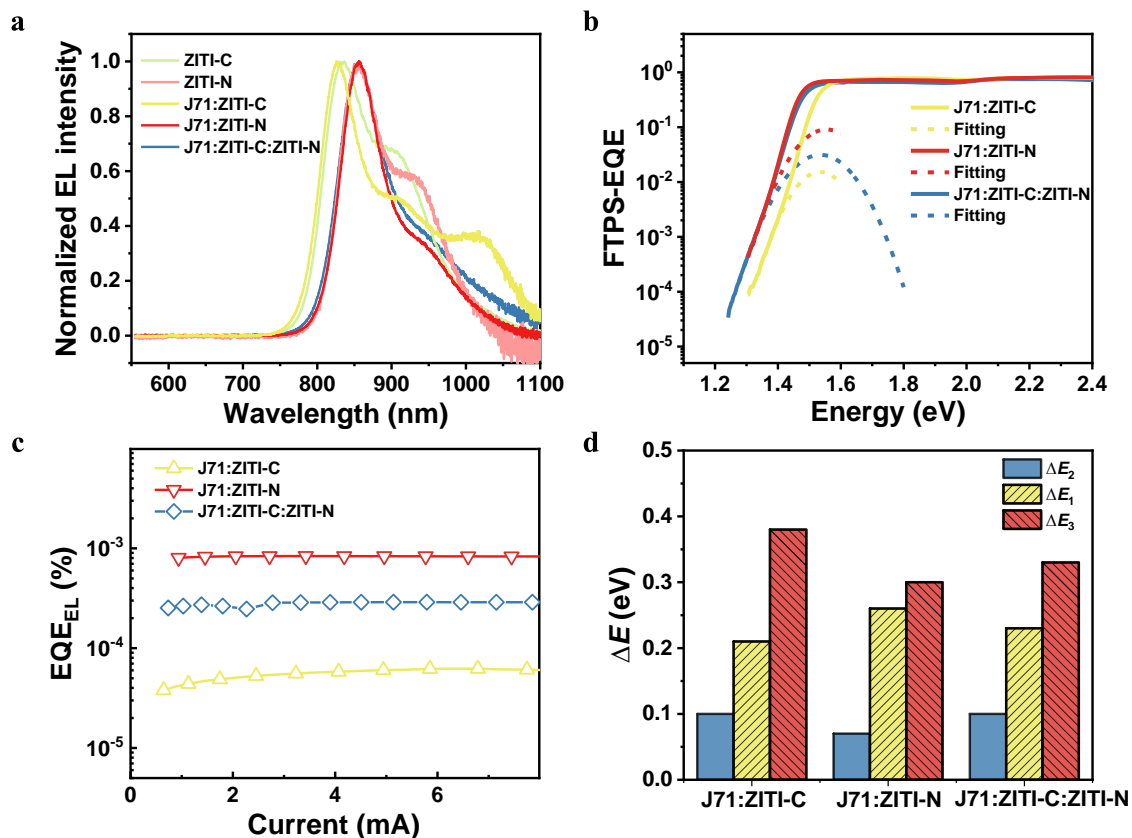
Figure S5. **Energy loss analysis.** (a) Electroluminescence spectra of devices based on the pristine NFA and blended films. (b) FTPS-EQE of the blended devices. (c) Normalized EQE_{EL}. (d) Energy loss: ΔE_1, ΔE_2 and ΔE_3 of J71:ZITI-C-, J71:ZITI-N-, and J71:ZITI-C:ZITI-N-based devices.
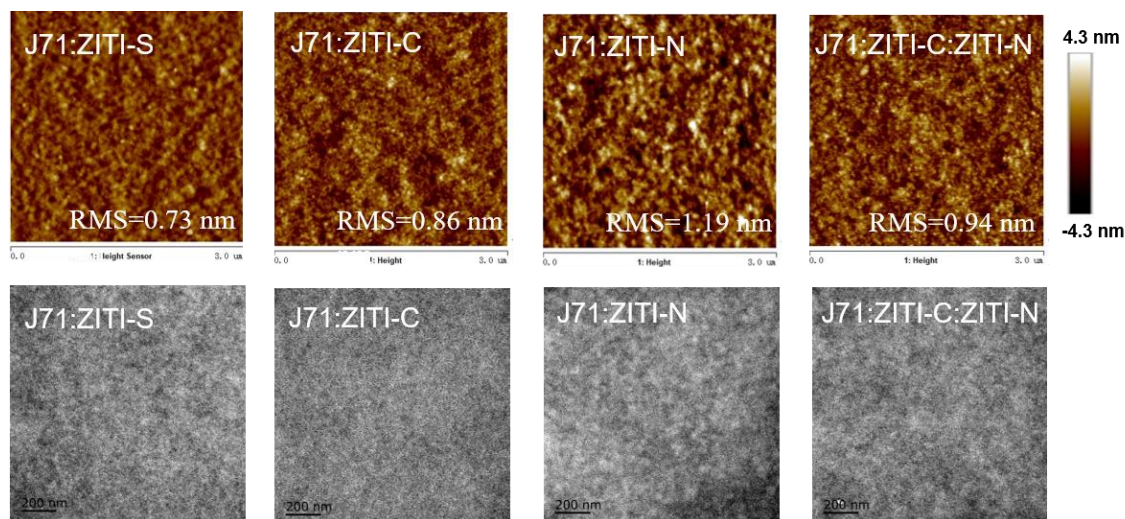
Figure S6. AFM height (3 × 3 μm) and TEM images of optimized blend films.
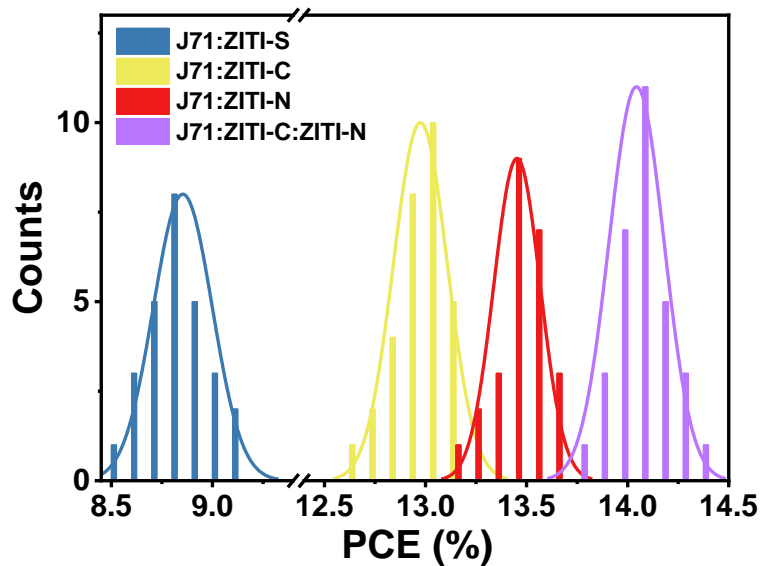
Figure S7. Histogram of the PCE measurements for 25 individual devices based on J71:ZITI-X blends.
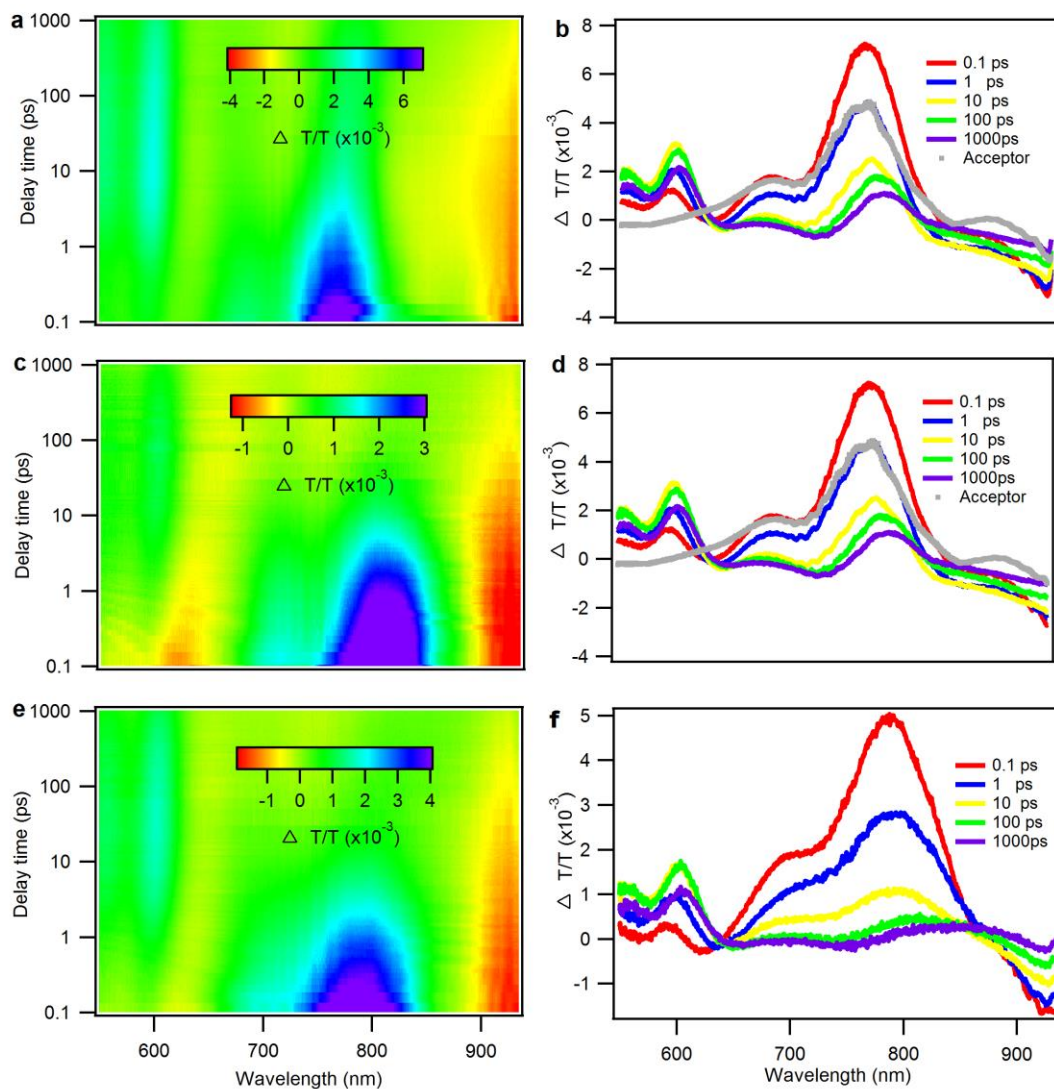
Figure S8. TAS investigation. Color plot of fs Transient absorption spectra of (a) J71:ZITI-C, (c) J71:ZITI-N and, (e) J71:ZITI-C:ZITI-N blend films at indicated delay times under 750 nm excitation with a fluence below 10 μJ/cm^2. Representative fs Transient absorption spectra of (b) J71:ZITI-C, (d) J71:ZITI-N, and (f) J71:ZITI-C:ZITI-N blend films at indicated delay time. Gray dots: TA spectrum of neat ZITI-C and ZITI-N film excited by 750 nm.
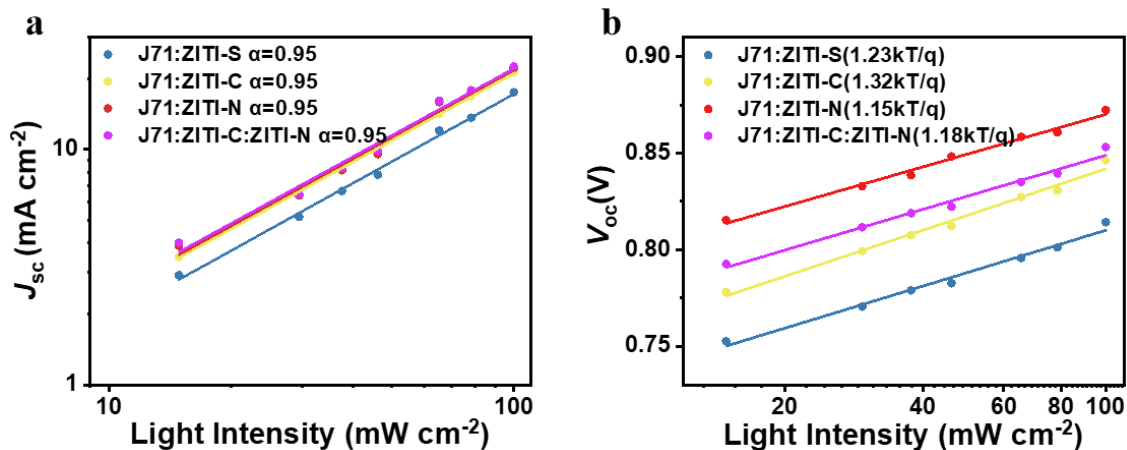
Figure S9. Charge recombination. (a) Measurement of J_{sc} versus light intensity. (b) V_{oc} versus light intensity for J71:ZITI-S-, J71:ZITI-C-, J71:ZITI-N-, and J71:ZITI-C:ZITI-N-based devices.
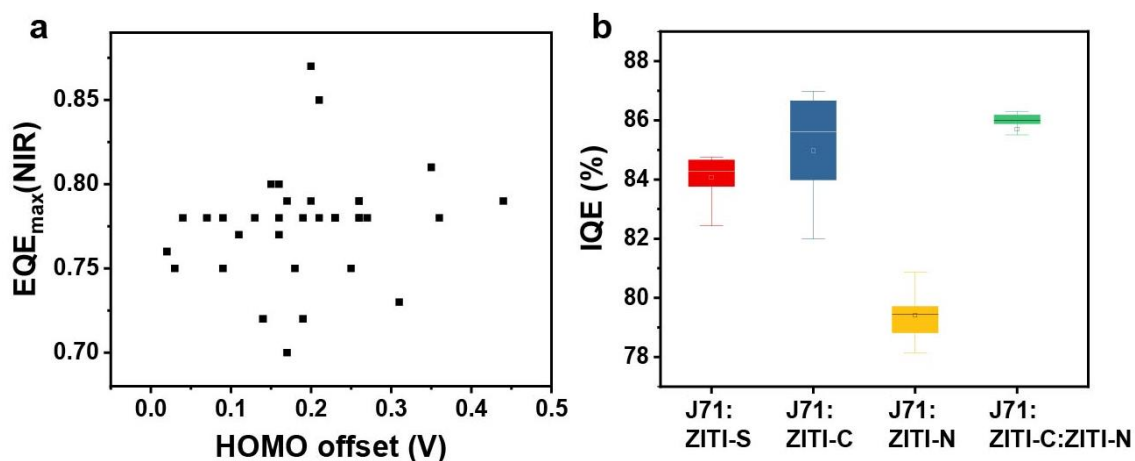
Figure S10. (a) EQE$_{max}$ in NIR region against HOMO offset plots of the reported organic solar cells with efficiencies over 12%. (b) IQE response of J71:ZITI-X-based devices with different HOMO offsets.

Table S1. Photovoltaic performance of J71:(ZITI-S/ZITI-C/ZITI-N)-based solar cells with different D/A ratio with device structure of ITO/PEDOT:PSS/active layer/PDINO/Al. The average values with standard deviations were obtained from 10 devices.

|	D:A	V_{oc} (V)	J_{sc} (mA cm^{-2})	FF (%)	PCE (%)
	1:0.7	0.813±0.002	16.70±0.20	60.18±0.76	8.17±0.15 (8.37)
J71:ZITI-S	1:1	0.812±0.004	17.18±0.38	63.51±0.87	8.86±0.18 (9.12)
	1:1.3	0.809±0.003	17.83±0.14	60.28±0.76	8.56±0.16 (8.81)
	1:0.7	0.856±0.003	20.38±0.29	70.83±0.67	12.56±0.12 (12.70)
J71:ZITI-C	1:1	0.851±0.006	21.28±0.26	72.03±0.79	13.02±0.13 (13.18)
	1:1.3	0.852±0.004	21.53±0.16	70.26±0.75	12.89±0.14 (13.13)
	1:0.7	0.876±0.002	22.13±0.19	67.96±0.93	13.19±0.21 (13.42)
J71:ZITI-N	1:1	0.873±0.005	21.73±0.33	70.96±0.88	13.47±0.12 (13.68)
	1:1.3	0.877±0.004	21.95±0.21	66.96±0.97	13.15±0.16 (13.30)

Table S2. Photovoltaic performance of J71:(ZITI-S/ZITI-C/ZITI-N)-based solar cells with different thicknesses. The average values with standard deviations were obtained from 10 devices.

	rpm	Thickness (nm)	V_{oc} (V)	J_{sc} (mA cm^{-2})	FF (%)	PCE (%)
	4000	90	0.815±0.003	16.57±0.28	63.65±0.63	8.64±0.13 (8.82)
J71:ZITI-S	3500	95	0.812±0.004	17.18±0.38	63.51±0.87	8.86±0.18 (9.12)
	3000	110	0.809±0.003	17.86±0.36	60.23±0.93	8.71±0.13 (8.90)
	2500	120	0.807±0.002	17.60±0.28	57.15±0.76	8.14±0.29 (8.38)
	3500	95	0.849±0.005	20.38±0.19	73.13±0.86	12.71±0.15 (12.99)
J71:ZITI-C	3000	110	0.851±0.006	21.28±0.26	72.03±0.79	13.02±0.13 (13.18)
	2500	120	0.850±0.004	21.08±0.17	70.98±0.83	12.99±0.16 (13.10)
	2000	135	0.847±0.003	21.37±0.25	69.88±0.73	12.94±0.12 (13.02)
	3500	95	0.876±0.004	21.19±0.12	70.89±0.75	13.23±0.15 (13.46)
J71:ZITI-N	3000	110	0.873±0.005	21.73±0.33	70.96±0.88	13.47±0.12 (13.68)
	2500	120	0.870±0.005	21.72±0.32	68.26±0.98	13.07±0.15 (13.21)

Table S3. Photovaltaic parameters of J71:(ZITI-S/ZITI-C/ZITI-N)-based devices before and after thermal annealing. The average values with standard deviations were obtained from 10 devices.

	TA	V_{oc} (V)	J_{sc} (mA cm^{-2})	FF (%)	PCE (%)
J71:ZITI-S	as-cast	0.835±0.003	16.37±0.21	54.27±0.86	7.42±0.20 (7.56)
	80℃/10 min	0.820±0.004	16.26±0.09	60.83±0.89	8.12±0.13 (8.23)
	100℃/10 min	0.812±0.004	17.18±0.38	63.51±0.87	8.86±0.18 (9.12)
	120℃/10 min	0.813±0.002	15.99±0.19	55.37±0.67	6.95±0.36 (7.30)
J71:ZITI-C	as-cast	0.899±0.005	19.58±0.24	66.53±0.74	11.64±0.12 (11.89)
	100℃/10 min	0.857±0.004	21.08±0.17	68.03±0.65	12.71±0.10 (12.87)
	120℃/10 min	0.851±0.006	21.28±0.26	72.03±0.79	13.02±0.13 (13.18)
	140℃/10 min	0.841±0.006	21.28±0.16	72.25±0.69	12.95±0.15 (13.09)
J71:ZITI-N	as-cast	0.913±0.004	20.73±0.29	61.61±0.74	11.68±0.15 (11.84)
	100℃/10min	0.883±0.002	21.93±0.21	65.07±0.86	12.66±0.22 (12.88)
	120℃/10min	0.873±0.005	21.73±0.33	70.96±0.88	13.47±0.12 (13.68)
	140℃/10 min	0.861±0.003	20.93±0.29	70.20±0.78	13.17±0.15 (13.28)

Table S4. Photovaltaic parameters of J71:ZITI-C:ZITI-N (D:A_1:A_2)-based devices. The average values with standard deviations were obtained from 20 devices.

D:A_1:A_2	V_{oc} (V)	J_{sc} (mA cm^{-2})	FF (%)	PCE (%)
1:1:0	0.851±0.006	21.28±0.26	72.03±0.79	13.02±0.13 (13.18)
1:0.7:0.3	0.851±0.003	22.62±0.32	70.32±0.88	13.54±0.17 (13.76)
1:0.6:0.4	0.858±0.006	22.73±0.24	70.29±1.07	13.56±0.20 (13.84)
1:0.5:0.5	0.857±0.004	23.01±0.24	71.72±0.98	14.05±0.21 (14.36)
1:0.4:0.6	0.861±0.004	22.43±0.23	72.17±0.67	13.92±0.16 (14.10)
1:0.3:0.7	0.865±0.006	22.39±0.33	70.76±0.78	13.70±0.16 (13.96)
1:0:1	0.873±0.005	21.73±0.36	70.96±0.88	13.47±0.12 (13.68)

Table S5. Charge transport properties of J71:ZITI-X blend films measured by SCLC method. The average values with standard deviations were obtained from 6 devices.

	μ_h (cm^2 V^{-1} s^{-1})	μ_e (cm^2 V^{-1} s^{-1})	μ_h:μ_e
J71:ZITI-S	2.75 (2.55±0.39)×10^{-4}	1.54 (1.46±0.17)×10^{-4}	1.78
J71:ZITI-C	3.83 (3.01±0.46)×10^{-4}	1.86 (1.83±0.35)×10^{-4}	2.05
J71:ZITI-N	2.69 (2.56±0.26)×10^{-4}	2.12 (2.01±0.27)×10^{-4}	1.27
J71:ZITI-C:ZITI-N	2.82 (2.69±0.43)×10^{-4}	2.24 (2.11±0.26)×10^{-4}	1.26

Table S6. Energy loss analysis.

	V_{oc} (V)	E_g^{opt} [a] (eV)	E_g^{inter} [b] (eV)	$q\Delta V_{oc}$ [c] ($q\Delta V_{oc}$) [d] (eV)	E_{CT} (eV)	ΔE_2 (eV)	ΔE_1 (eV)	EQE$_{EL}$ (%)	ΔE_3 (eV)
J71:ZITI-S	0.81	1.61	1.66	0.80 (0.85)	1.36	0.30	0.20	2.54×10^{-5}	0.39
J71:ZITI-C	0.85	1.47	1.55	0.62 (0.70)	1.45	0.1	0.21	4.39×10^{-5}	0.38
J71:ZITI-N	0.88	1.41	1.51	0.53 (0.63)	1.44	0.07	0.26	8.16×10^{-4}	0.30
J71:ZITI-C:ZITI-N	0.86	1.41	1.51	0.55 (0.65)	1.41	0.1	0.23	2.64×10^{-4}	0.33

[a] E_g^{opt} is determined by thin-film absorption onset of an acceptor; [b] E_g^{inter} is determined at the intersection between absorption and emission of blend films; [c] $q\Delta V_{oc}=E_g^{opt}-qV_{oc}$; [d] $q\Delta V_{oc}=E_g^{inter}-qV_{oc}$.

Table S7. Photovoltaic performance of J71:ZITI-C:ZITI-N-based solar cells with different thicknesses. The average values with standard deviations were obtained from 10 devices.

	rpm	Thickness (nm)	V_{oc} (V)	J_{sc} (mA cm^{-2})	FF (%)	PCE (%)
J71:ZITI-C:ZITI-N =1:0.5:0.5	3500	95	0.854±0.005	22.88±0.17	72.07±0.67	13.85±0.24 (14.06)
	3000	110	0.857±0.004	23.01±0.24	71.72±0.98	14.05±0.21 (14.36)
	2500	120	0.853±0.004	22.95±0.16	69.94±0.68	13.79±0.21 (13.94)

Table S8. The EQE$_{max}$ in NIR region against HOMO offset plots of the reported organic solar cells with efficiencies over 12%.

Active layer	PCE$_{max}$ (%)	ΔE_{HOMO} (V)	NIR EQE$_{max}$	Reference
PBDB-T-2Cl:IT-4F	14.40	0.15	80%	1
PBDB-TF:ITPN	12.60	0.21	78%	2
PBT1-C:ITCPTC	12.80	0.16	77%	3
PBDB-T:F-Br	12.05	0.44	79%	4
PTQ10:IDIC	12.70	0.20	79%	5
PTB7-Th:IEICO-4F	12.80	0.20	87%	6
PBT1-C:TBTTT-2F	12.03	0.26	79%	7
PTQ10:IDTPC	12.20	0.26	78%	8
J71:ITCPTC	12.54	0.17	70%	9
J71:ZITI	13.24	0.11	77%	10
PBDTS-Se-TAZ:ITIC	12.31	0.19	78%	11
PTQ10:m-ITIC-4F	12.53	0.19	78%	12
PBDB-TF:IT-4F	13.70	0.13	78%	13
PDTB-EF-T:IT-4F	14.20	0.16	78%	14
PBDB-T-SF:NCBDT-4Cl	14.10	0.18	75%	15
PBDB-T:SN6IC-4F	13.20	0.19	72%	16
PBDB-T:IDT8CN-M	12.43	0.27	78%	17
PBDB-T:C8-ITIC	13.20	0.16	80%	18
PM7:IT-4F	13.10	0.17	79%	19
FTAZ: IOIC2	12.30	0.03	75%	20
PBDB-T:BDTThIT-M	12.12	0.04	78%	21
PBDTS-TDZ:ITIC	12.80	0.09	75%	22
PBDB-T-SF:IT-4F	13.10	0.26	79%	23
FTAZ:ITIC-Th1	12.10	0.36	78%	24
PBDB-T:NITI	12.74	0.35	81%	25
PBDB-TF:IDTN	12.20	0.31	73%	26
PBDB-T:IT-M	12.05	0.25	75%	27
PM6:Y6	15.70	0.09	78%	28
PTQ10:IE4F-S	12.20	0	68%	29
PBDB-T:IE4F-S	13.72	0.21	85%	29
J101:ZITI	14.43	0.23	78%	30
PDCBT:PDCBT-Cl	12.38	0.14	72%	31

PM7:IXIC-2Cl	13.72	0.07	78%	32
PBDB-T:BTTIC	13.18	0.26	78%	33
PCE10:3TT-OCIC	12.43	0.02	76%	34
PBDB-TF:BTP-4Cl	16.50	0.23	78%	35

Table S9. The photovoltaic parameters of J71:ZITI-N-based devices with different treatments.

Treatments	V_{oc} (V)	J_{sc} (mA cm^{-2})	FF (%)	PCE (%)
as-cast	0.913	20.73	61.61	11.84
120℃/10 min	0.876	21.78	72.00	13.68
0.5% DIO	0.951	12.33	42.84	5.03
0.5% 1-CN	0.970	11.08	50.28	5.41
CF 30s	0.919	20.82	63.38	12.13
THF 30s	0.905	20.85	63.14	11.92
CS2 30s	0.906	21.68	60.72	11.93

Table S10. The photovoltaic parameters of PBDB-TF:ZITI-C-, PBDB-TF:ZITI-N- and PBDB-TF:ZITI-C:ZITI-N-based devices.

Active layer	Treatments	V_{oc} (V)	J_{sc} (mA cm^{-2})	FF (%)	PCE (%)
PBDB-TF:ZITI-C	as-cast	0.934	20.00	65.82	12.31
	60℃/10 min	0.927	20.25	69.87	13.12
	100℃/10 min	0.903	20.47	67.25	12.43
	120℃/10 min	0.872	19.89	63.56	11.03
PBDB-TF:ZITI-N	as-cast	0.939	17.36	47.71	7.78
	60℃/10min	0.933	18.90	59.72	10.52
	80℃/10min	0.926	19.36	61.13	10.96
	120℃/10min	0.907	21.52	67.98	13.28
PBDB-TF:ZITI-C:ZITI-N=1:0.5:0.5	as-cast	0.942	19.98	63.17	11.89
	80℃/10 min	0.917	20.94	65.53	12.58
	100℃/10 min	0.905	21.40	67.88	13.15
	120℃/10 min	0.892	21.72	71.36	13.83

Table S 11. The photovoltaic parameters of polymer: ZITI-N-based devices.

Donor	treatment	V_{oc} (V)	J_{sc} (mA cm^{-2})	FF (%)	PCE (%)
PBDB-T-F	as-cast	0.939	17.36	47.71	7.78
	120℃/10 min	0.907	21.52	67.98	13.28

PBDB-T	as-cast	0.891	20.04	61.93	11.06
	120℃/10 min	0.839	22.20	70.74	13.17
PTB7-Th	as-cast	0.779	20.17	60.42	9.49
	120℃/10 min	0.764	21.17	69.92	11.31

Table S 12. The photovoltaic parameters of J71:ZITI-C:ZITI-N-based devices with different thickness.
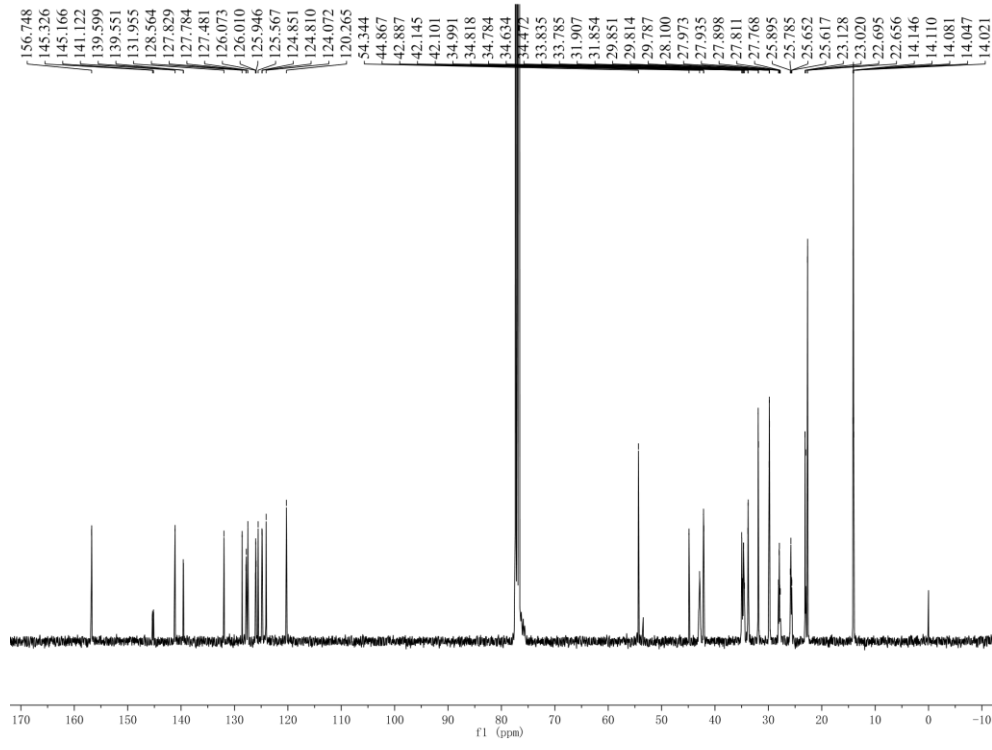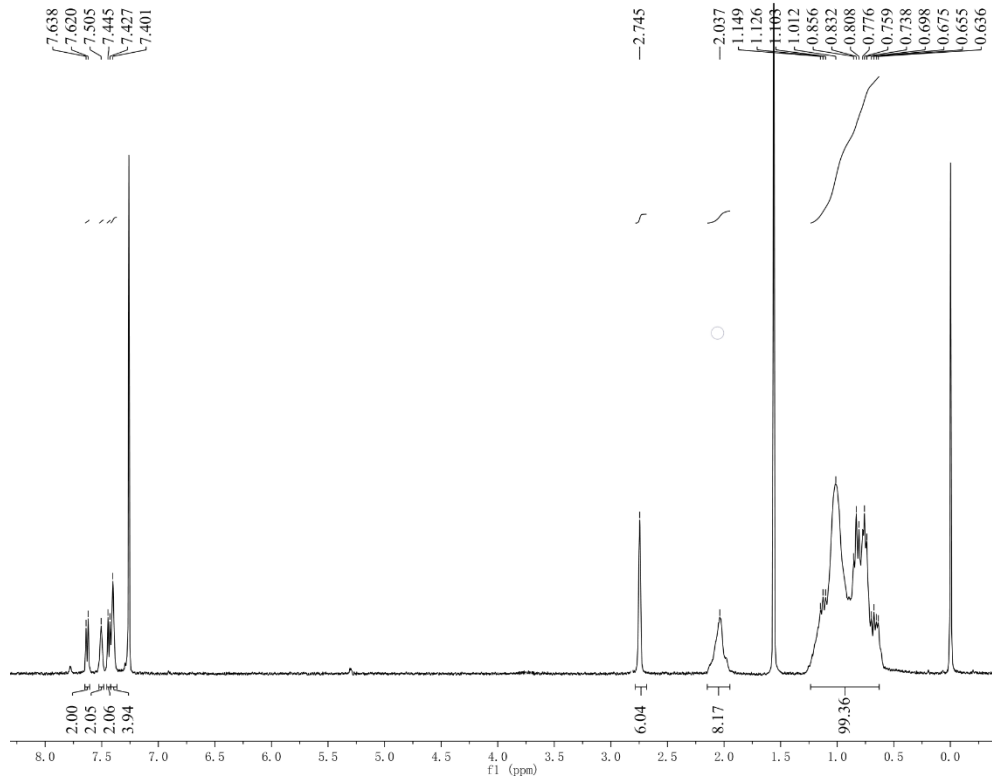
Thickness (nm)	V_{oc} (V)	J_{sc} (mA cm^{-2})	FF (%)	PCE (%)
95	0.854	22.88	72.07	14.06
110	0.857	23.01	71.72	14.36
120	0.853	22.95	69.94	13.94
170	0.847	22.49	65.03	12.39
200	0.842	22.33	64.58	12.05

1. Zhang, S., Qin, Y., Zhu, J., and Hou, J. (2018). Over 14% efficiency in polymer solar cells enabled by a chlorinated polymer donor. Adv. Mater. *30*, 1800868.

2. Yu, R., Yao, H., Hong, L., Xu, Y., Gao, B., Zhu, J., Zu, Y. and Hou, J. (2018). Enhancing the photovoltaic performance of nonfullerene acceptors via conjugated rotatable end groups. Adv. Energy Mater. *8*, 1802131.

3. Xiong, W. *et al.* (2018). Controlling molecular weight to achieve high-efficient polymer solar cells with unprecedented fill factor of 79% based on non-fullerene small molecule acceptor. Sol. RRL *2*, 1800129.

4. Wang, Y. *et al.* (2018). A halogenation strategy for over 12% efficiency nonfullerene organic solar cells. Adv. Energy Mater. *8*, 1702870.

5. Sun, C., Pan, F., Bin, H., Zhang, J., Xue, L., Qiu, B., Wei, Z., Zhang, Z. G., and Li, Y. (2018). A low cost and high performance polymer donor material for polymer solar cells. Nat. Commun. *9*, 743.

6. Song, X., Gasparini, N., Ye, L., Yao, H., Hou, J., Ade, H., and Baran, D. (2018). Controlling blend morphology for ultrahigh current density in nonfullerene acceptor-based organic solar cells. ACS Energy Lett. *3*, 669-676.

7. Song, J., Li, C., Ye, L., Koh, C., Cai, Y., Wei, D., Woo, H. Y., Sun, Y. (2018). Extension of indacenodithiophene backbone conjugation enables efficient asymmetric a–d–a type non-fullerene acceptors. J. Mater. Chem. A *6*, 18847-18852.

8. Luo, Z., Sun, C., Chen, S., Zhang, Z., Wu, K., Qiu, B., Yang, C., Li, Y., and Yang, C. (2018). Side-chain impact on molecular orientation of organic semiconductor acceptors: High performance nonfullerene polymer solar cells with thick active layer over 400 nm. Adv. Energy Mater. *8*, 1800856.

9. Luo, Z. *et al.* (2018). Fine-tuning of molecular packing and energy level through methyl substitution enabling excellent small molecule acceptors for nonfullerene polymer solar cells with efficiency up to 12.54. Adv. Mater. *30*, 1706124.

10. Liu, W., Zhang, J., Zhou, Z., Zhang, D., Zhang, Y., Xu, S., and Zhu, X. (2018). Design of a new fused-ring electron acceptor with excellent compatibility to wide-bandgap polymer donors for high-performance organic photovoltaics. Adv. Mater. *30*, 1800403.
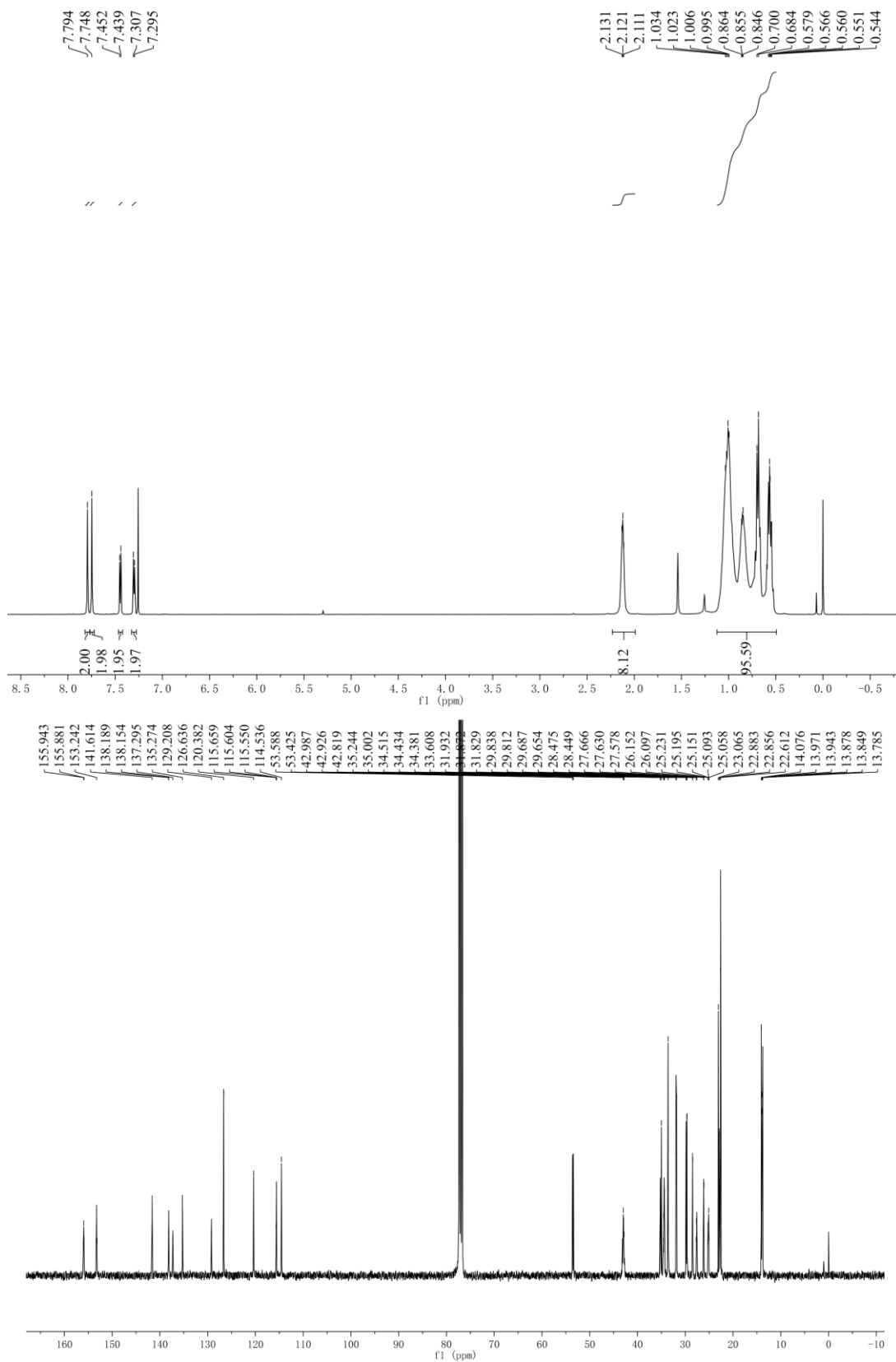
11. Li, Z., Xu, X., Zhang, G., Yu, T., Li, Y., and Peng, Q. (2018). Highly efficient non-fullerene polymer solar cells enabled by wide bandgap copolymers with conjugated selenyl side chains. Sol. RRL *2*, 1800186.

12. Li, X. J. *et al.* (2018). Improvement of photovoltaic performance of polymer solar cells by rational molecular optimization of organic molecule acceptors. Adv. Energy Mater. *8*, 1800815.

13. Li, W., Ye, L., Li, S., Yao, H., Ade, H., Hou, J. A high-efficiency organic solar cell enabled by the strong intramolecular electron push-pull effect of the nonfullerene acceptor. *Adv. Mater.* **30**, 1707170 (2018).

14. Li, S., Ye, L., Zhao, W., Yan, H., Yang, B., Liu, D., Li, W., Ade, H., and Hou, J. (2018). A wide band gap polymer with a deep highest occupied molecular orbital level enables 14.2% efficiency in polymer solar cells. J. Am. Chem. Soc. *140*, 7159-7167.

15. Kan, B., Feng, H., Yao, H., Chang, M., Wan, X., Li, C. X., Hou, J., and Chen, Y. (2018). A chlorinated low-bandgap small-molecule acceptor for organic solar cells with 14.1% efficiency and low energy loss. Sci. China Chem. *61*, 1307-1313.

16. Huang, C. *et al.* (2018). Highly efficient organic solar cells based on s,n-heteroacene non-fullerene acceptors. Chem. Mater. *30*, 5429-5434.

17. Gao, W. *et al.* (2018). Asymmetrical small molecule acceptor enabling nonfullerene polymer solar cell with fill factor approaching 79%. ACS Energy Lett. *3*, 1760-1768.

18. Fei, Z. *et al.* (2018). An alkylated indacenodithieno[3,2-b]thiophene-based nonfullerene acceptor with high crystallinity exhibiting single junction solar cell efficiencies greater than 13% with low voltage losses. Adv. Mater. *30*, 1705209.

19. Fan, Q. *et al.* (2018). Chlorine substituted 2d-conjugated polymer for high-performance polymer solar cells with 13.1% efficiency via toluene processing. Nano Energy *48*, 413-420.

20. Zhu, J. *et al.* (2018). Naphthodithiophene-based nonfullerene acceptor for high-performance organic photovoltaics: Effect of extended conjugation. Adv. Mater. *30*, 1704713.

21. An, Q. *et al.* (2018). Energy level modulation of non-fullerene acceptors enables efficient organic solar cells with small energy loss. J. Mater. Chem. A *6*, 2468-2475.

22. Xu, X., Yu, T., Bi, Z., Ma, W., Li, Y., and Peng, Q. (2018). Realizing over 13% efficiency in green-solvent-processed nonfullerene organic solar cells enabled by 1,3,4-thiadiazole-based wide-bandgap copolymers. Adv. Mater. *30*, 1703973.

23. Zhao, W., Li, S., Yao, H., Zhang, S., Zhang, Y., Yang, B., Hou, J. Molecular optimization enables over 13% efficiency in organic solar cells. *J. Am. Chem. Soc.* **139**, 7148-7151 (2017).

24. Zhao, F. *et al.* (2017). Single-junction binary-blend nonfullerene polymer solar cells with 12.1% efficiency. Adv. Mater. *29*, 1700144.

25. Xu, S., Zhou, Z., Liu, W., Zhang, Z., Liu, F., Yan, H., and Zhu, X. (2017). A twisted thieno[3,4-*b*]thiophene-based electron acceptor featuring a 14-π-electron indenoindene core for high-performance organic photovoltaics. Adv. Mater. *29*, 1704510.

26. Li, S., Ye, L., Zhao, W., Liu, X., Zhu, J., Ade, H., and Hou, J. (2017). Design of a new small-molecule electron acceptor enables efficient polymer solar cells with high fill factor. Adv. Mater. *29*, 1704051.

27.   Li, S., Ye, L., Zhao, W., Zhang, S., Mukherjee, S., Ade, H., and Hou, J. (2016). Energy-level modulation of small-molecule electron acceptors to achieve over 12% efficiency in polymer solar cells. Adv. Mater. *28*, 9423-9429.

28.   Yuan, J. *et al.* (2019). Single-junction organic solar cell with over 15% efficiency using fused-ring acceptor with electron-deficient core. Joule *3*, 1140-1151.

29.   Zou, Y., Dong, Y., Sun, C., Wu, Y., Yang, H., Cui, C., and Li, Y. (2019). High-performance polymer solar cells with minimal energy loss enabled by a main-chain-twisted nonfullerene acceptor. Chem. Mater. *31*, 4222-4227.

30.   Wang, T. *et al.* (2019). A wide-bandgap d–a copolymer donor based on a chlorine substituted acceptor unit for high performance polymer solar cells. J. Mater. Chem. A *7*, 14070-14078.

31.   Wang, Q., Li, M., Zhang, X., Qin, Y., Wang, J., Zhang, J., Hou, J., Janssen, R. A. J., and Geng, Y. Carboxylate-substituted polythiophenes for efficient fullerene-free polymer solar cells: The effect of chlorination on their properties. Macromolecules DOI: 10.1021/acs.macromol.9b00793.

32.   Liu, T. *et al.* A nonfullerene acceptor with 1000 nm absorption edge enables ternary organic solar cells with improved optical and morphological properties and efficiencies over 15%. Energy Environ. Sci. DOI: 10.1039/C9EE01030K.

33.   Liu, T. *et al.* (2019). A high-performance non-fullerene acceptor compatible with polymers with different bandgaps for efficient organic solar cells. Sol. RRL *3*, 1800376.

34.   Gao, H. H. *et al.* Achieving both enhanced voltage and current through fine-tuning molecular backbone and morphology control in organic solar cells. Adv. Energy Mater. DOI: 10.1002/aenm.201901024.

35.   Cui, Y. *et al.* (2019). Over 16% efficiency organic photovoltaic cells enabled by a chlorinated acceptor with increased open-circuit voltages. Nat. Commun. *10*, 2515.
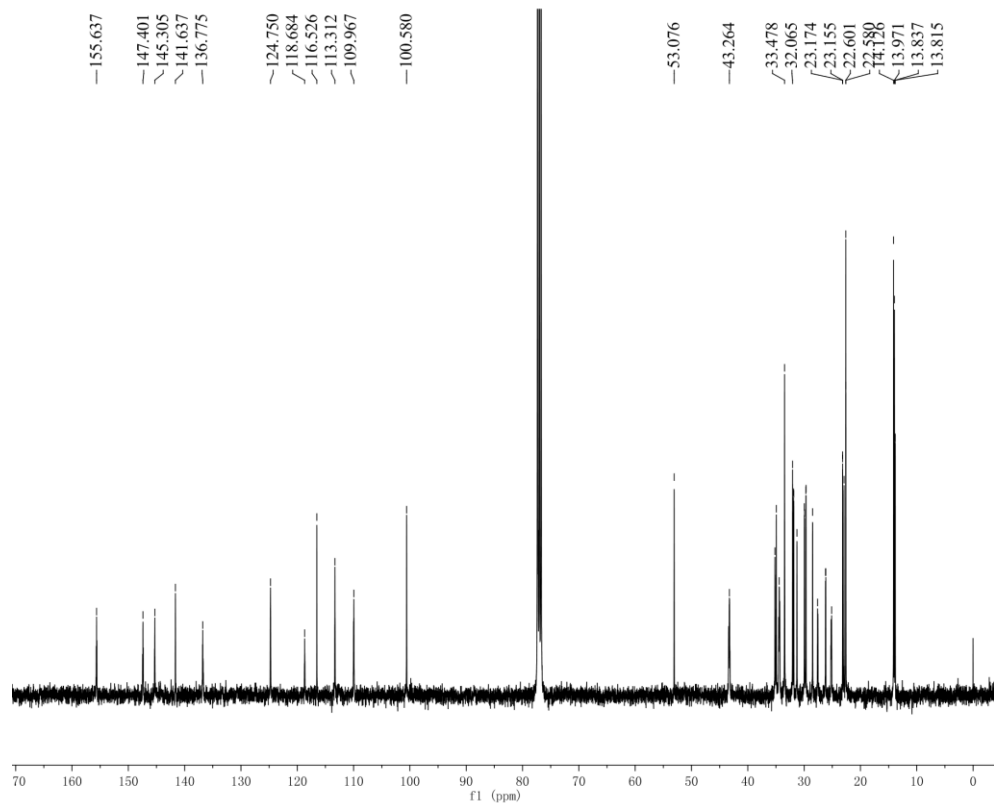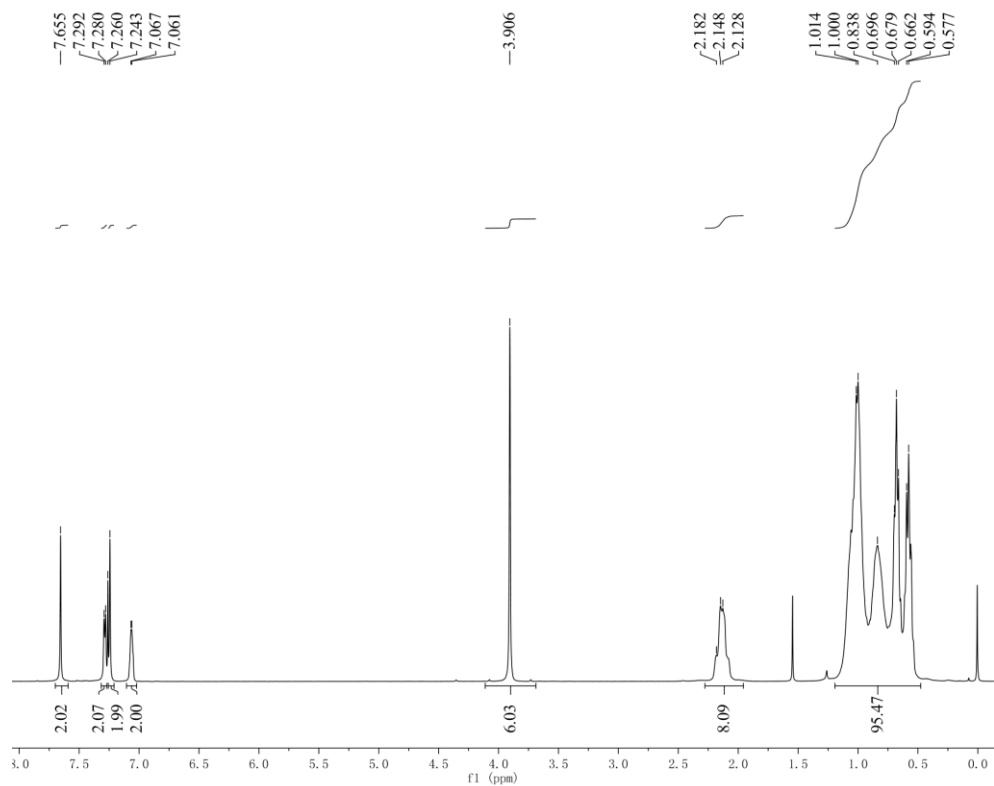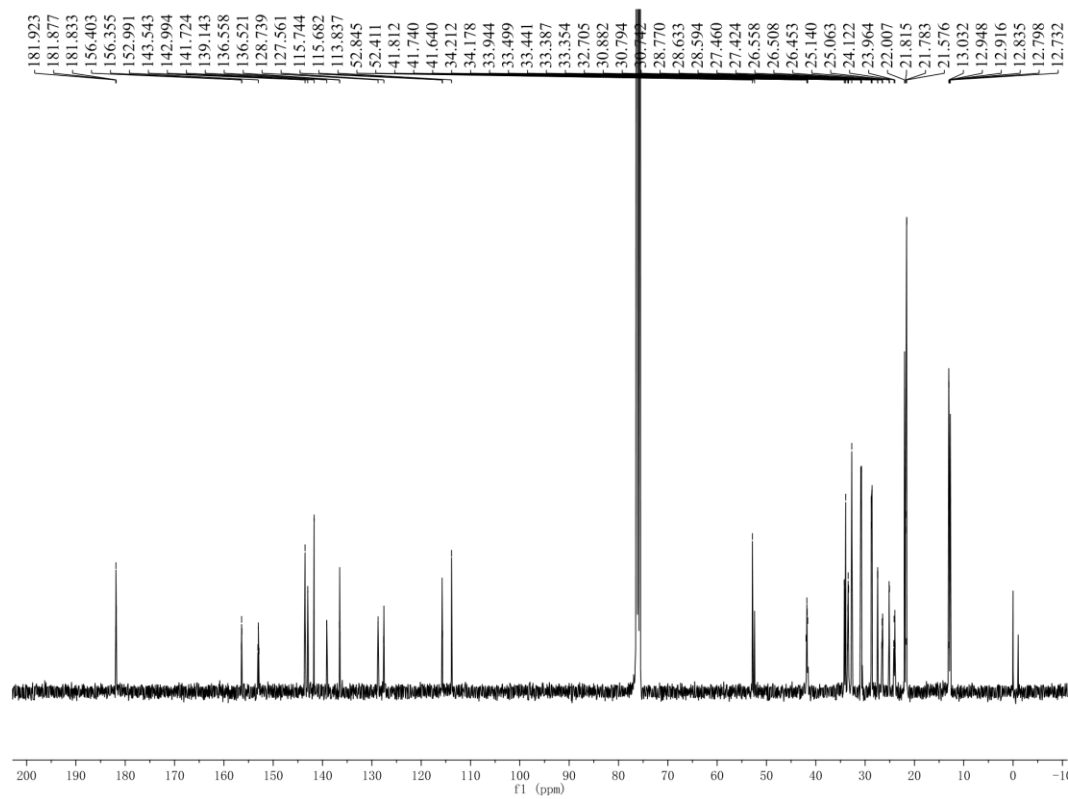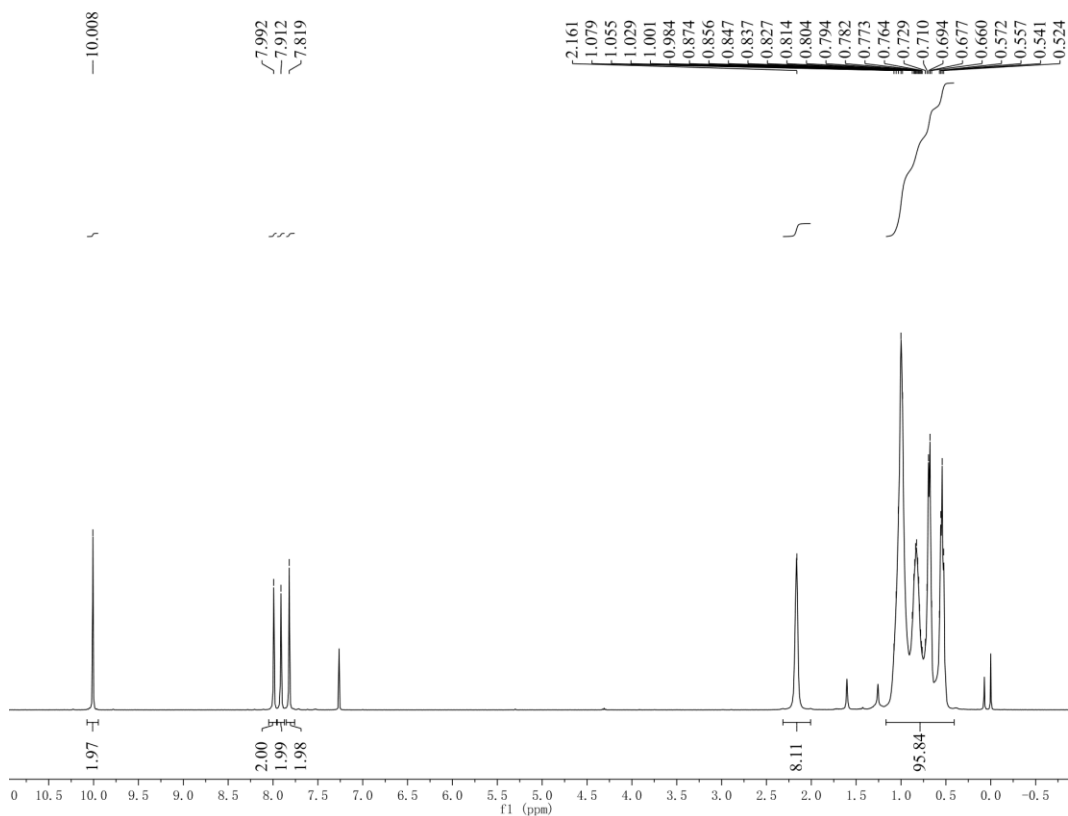
NMR Charts
Compound 2

Compound IIDT-S

7.794
7.748
7.452
7.439
7.307
7.295

2.131
2.121
2.111
1.034
1.023
1.006
0.995
0.864
0.855
0.846
0.700
0.684
0.579
0.566
0.560
0.544

155.943
155.881
153.242
141.614
138.189
138.154
137.295
135.274
129.208
126.636
120.382
115.659
115.604
115.550
114.536
53.588
53.425
42.987
42.926
42.819
35.244
35.002
34.515
34.434
34.381
33.608
31.932
31.829
29.838
29.812
29.687
29.654
28.475
28.449
27.666
27.630
27.578
26.152
26.097
25.231
25.195
25.151
25.093
25.058
23.065
22.883
22.856
22.612
14.076
13.971
13.943
13.878
13.849
13.785

Compound IIDT-N

Compound 5-S

Compound 5-N
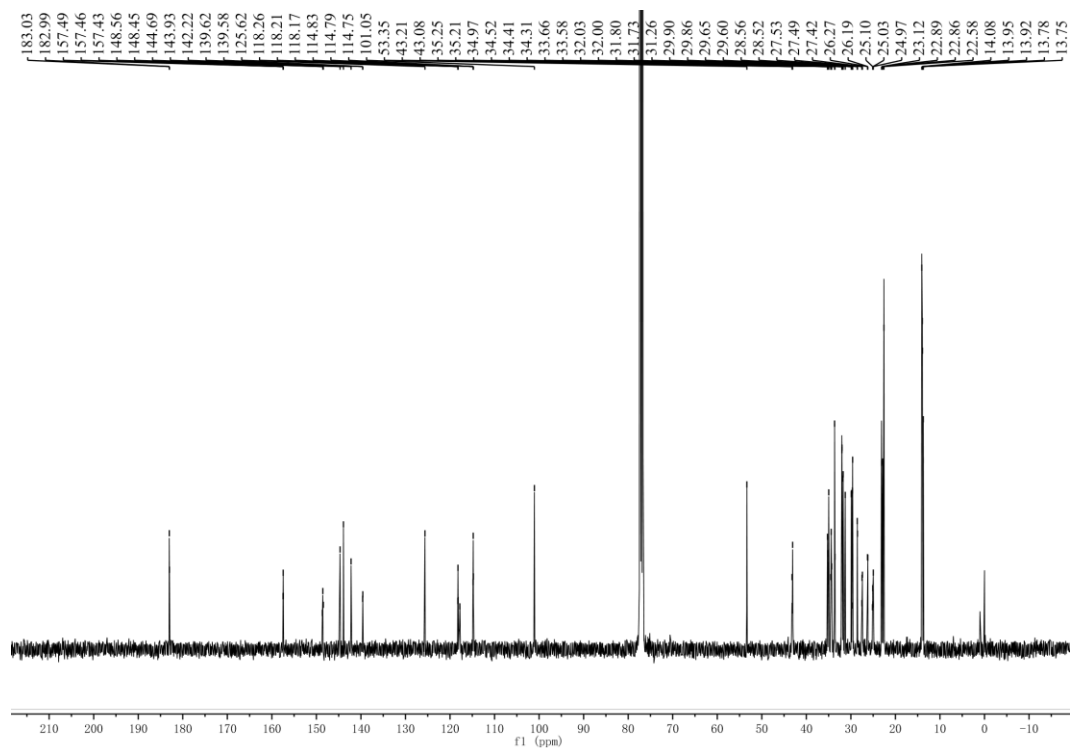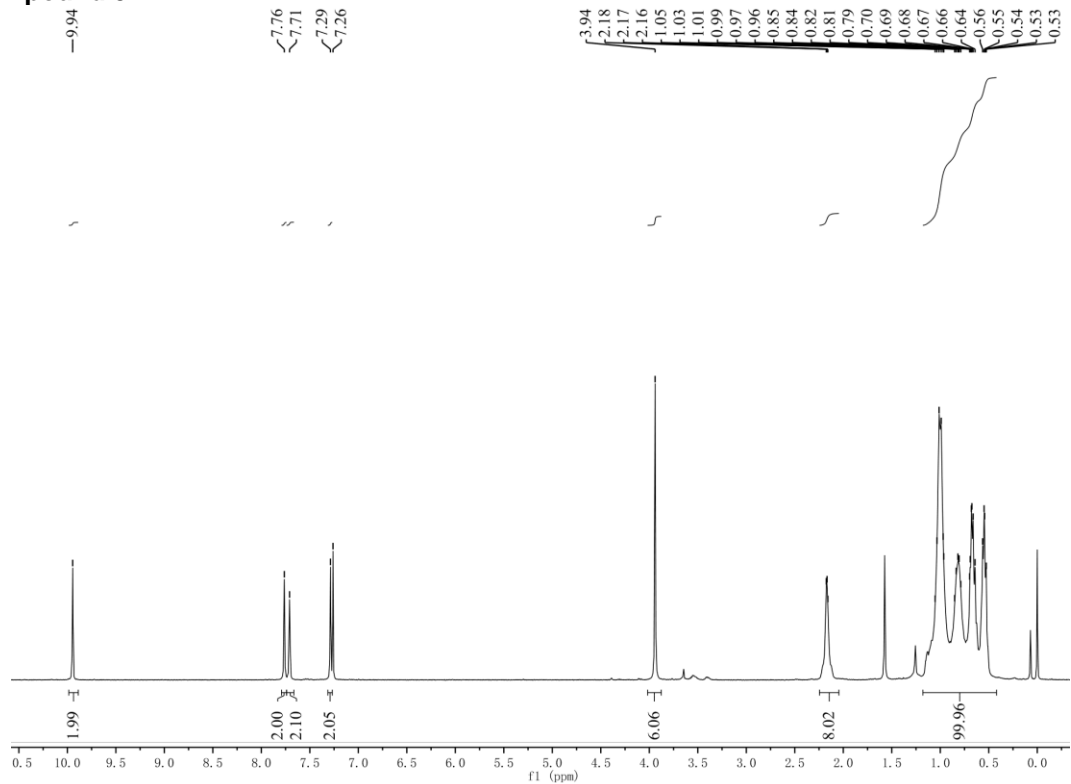
Compound ZITI-S

Compound ZITI-C

^{1}H NMR spectrum (top) with peaks at 8.964, 8.561, 8.545, 8.537, 8.520, 7.921, 7.787, 7.700, 7.681, 7.663, 7.565, 7.260, 3.880, 2.128, 1.548, 1.072, 1.000, 0.904, 0.845, 0.732, 0.719, 0.704, 0.591, 0.578, −0.001; integrations: 2.00, 1.98, 1.99, 2.02, 2.05, 1.97, 3.99, 8.05, 2.64, 94.55

^{13}C NMR spectrum (bottom) with peaks at 185.50, 164.48, 158.44, 158.20, 156.45, 154.76, 154.66, 153.02, 152.93, 147.88, 142.07, 139.39, 138.05, 136.09, 134.08, 133.90, 119.50, 116.75, 116.38, 114.47, 114.33, 114.07, 114.01, 111.96, 111.84, 76.50 CDCl, 76.28, 68.14, 53.67, 34.67, 34.38, 34.11, 33.35, 33.06, 31.45, 31.34, 31.30, 29.33, 29.18, 27.87, 27.19, 27.11, 25.61, 25.56, 24.81, 24.70, 22.56, 22.34, 22.14, 22.10, 13.54, 13.47, 13.30

Compound ZITI-N